DELFT UNIVERSITY OF TECHNOLOGY

REPORT 15-07

Efficient simulation of one-dimensional two-phase flow with a new high-order Discontinuous Galerkin method

J.S.B. van Zwieten, B. Sanderse, M.H.W. Hendrix, C. Vuik, R.A.W.M. Henkes

Abstract

One-dimensional models for multiphase flow in pipelines are commonly discretised using first-order Finite Volume (FV) schemes, often combined with implicit time-integration methods. While robust, these methods introduce much numerical diffusion depending on the number of grid points. In this paper we propose a high-order, space-time Discontinuous Galerkin (DG) Finite Element method with h-adaptivity to improve the efficiency of one-dimensional multiphase flow simulations. For smooth initial boundary value problems we show that the DG method converges with the theoretical rate and that the growth rate and phase shift of small, harmonic perturbations exhibit superconvergence. We employ two techniques to accurately and efficiently represent discontinuities. Firstly artificial diffusion in the neighbourhood of a discontinuity suppresses spurious oscillations. Secondly local mesh refinement allows for a sharper representation of the discontinuity while keeping the amount of work required to obtain a solution relatively low. The proposed DG method is shown to be superior to FV.

1 Introduction

Multiphase flow plays an important role in many industrial applications, such as in the petroleum and nuclear industry. In the petroleum industry a typical example of multiphase flow is the transport of oil and gas through long multiphase pipeline systems. For the design and optimization of such systems it is important to accurately predict the pressure and flow rate of both oil and gas along the pipeline as a function of time. An important example is the prediction of slug flow, which has a large influence on the sizing of receiving facilities at the outlet of the pipeline such as slug catchers or separators. A slug is a pocket of liquid that fully covers the pipe cross sectional area and that moves with relatively high velocity along the pipeline. Some slugs are initiated due to a flow instability at the gas/liquid interface of stratified flow in the pipeline, which marks the transition from stratified flow to hydrodynamic slug flow. The motion of these slugs, and of oil and gas in general, is governed by partial differential equations describing conservation of mass, momentum and energy. However, for oil and gas pipelines the numerical solution of these equations in three dimensions is prohibitively expensive due to the multi-scale nature of the problem: the pipeline length can be of the order of 100 kilometre, whereas the size of oil droplets or gas bubbles can be of the order of millimetres. In order to obtain a computationally tractable model which retains the most important physical effects, averaging techniques are typically applied to the governing equations, leading to a one-dimensional model. The one-dimensional two-fluid model (Stewart and Wendroff, 1984; Ishii and Hibiki, 2011) is the most commonly used model to simulate two-phase flow in pipelines or channels. It is capable of describing the transition from stratified flow to slug flow (Issa and Kempf, 2003). As such, the two-fluid model is a slug-capturing model in which slugs are a result of growing hydrodynamic instabilities.

Numerical solutions to the two-fluid model equations are in general obtained by finite difference methods or finite volume methods, both in commercial codes such as OLGA (Bendiksen et al., 1991) and LedaFlow as well as in academic

research codes (Issa and Kempf, 2003; Evje and Flåtten, 2003; Liao et al., 2008; Holmås, 2008; Fullmer et al., 2014). These finite difference and finite volume methods are almost exclusively first order in space and time. For example, the slug capturing code TRIOMPH from Issa and Kempf (2003) uses a finite volume method on a staggered grid, being first order accurate both in space and time. A main reason for the use of first order schemes is related to the ill-posedness of the basic two-fluid model (when surface tension or hydrostatic pressure variation are not taken into account) and its non-conservative nature. These properties make the application of high-order methods as developed for single-phase flow (such as Essentially Non-Oscillatory (ENO) schemes) non-trivial. The artificial diffusion introduced by first order methods effectively regularizes the differential equations through damping non-physical instabilities associated with ill-posedness (Fullmer et al., 2013). However, a major disadvantage of first order methods is that any physical instabilities will also be damped due to excessive numerical diffusion (Liao et al., 2008). As a result, very fine meshes are required (see e.g. Issa and Kempf (2003)); Bonizzi and Issa (2003) recommend that the grid size should be less than half of the diameter of the pipe to capture the natural growth of disturbances. For practical pipeline simulations this is computationally far too expensive.

A few studies on the use of high-order methods for the numerical solution of the two-fluid model have been performed. Holmås et al. (2008) use a pseudo-spectral Fourier method to solve the two-fluid model and indicate a gain in computational time of several orders of magnitude with respect to classical finite difference schemes; especially the first order upwind method has excessive numerical diffusion. Fullmer et al. (2013) show improved accuracy of a second order method over a first order method, although the second order method leads to non-monotone results. In all cases, these high-order upwind schemes can have unfavourable stability properties (Liao et al., 2008), giving a numerical growth rate which is quite different from the physical growth rate of instabilities. Consequently, high-order methods are not yet commonly applied for solving the two-fluid model equations.

The purpose of this paper is to present an efficient high-order numerical method that can simulate stratified and slug flow by solving the compressible two-fluid model. To overcome the common issues associated with high-order methods we propose an h-adaptive space-time Discontinuous-Galerkin Finite Element Method (DGFEM) scheme. This method allows a mesh to be refined locally (h-refinement). In smooth regions of the flow a coarse mesh is used, while a fine mesh is used to resolve the physics around sharp gradients, such as near a slug front or tail, or when the flow becomes locally single phase. This is believed to lead to a more efficient numerical method compared to classical low-order finite difference or finite volume methods on fixed grids. The scheme can be extended to include p-coarsening near discontinuities.

Several quite different adaptive space-time DG methods with adaptive refinement have been described. The tent-pitcher algorithm (Üngör and Sheffer, 2000; Abedi et al., 2010) creates a partial ordering of unstructured elements in space-time such that a discrete system can be solved on each element solely based on boundary data from lower elements in the partial ordering. Multiple elements can be solved for simultaneously if they are independent of each other. Since all characteristics should exit an element face in the same direction, this would yield very flat elements (in time) if the eigenvalues of the system have a

4

very large positive and negative component.

Another technique proposed by Gassner et al. (2015) involves a set elements of that are unstructured in space and extruded in time, where the time length of an element is variable. The flux contribution to an element is applied seperately from the volume contribution after the volume contributions of all neighbouring elements have been computed. The scheme allows local *h*- and *p*-adaptation. Since this method is essentially explicit, the time length restriction is severe for problems with very large characteristic speeds.

For a multidimensional multiphase flow application Sollie et al. (2011) use a structured space-time base mesh subdivided in time-slabs, a sequence of sets of elements with the same time interval. A discrete system is solved per time-slab using an explicit integration scheme for pseudo time. Coarse elements in which there is an interface, described by a level set on the coarse mesh, are subdivided, allowing locally unstructured elements, such that the interface matches element boundaries. This front tracking scheme requires several iterations to recompute the refinement as the level set depends on the flow field and vice versa. In one-dimensional multiphase flow applications this scheme requires, in absence of a level set, a non-trivial mechanism to locate jumps in the liquid hold-up *within* an element.

Fidkowski and Luo (2011) describe an adjoint based adaptive space-time DG scheme for the compressible Navier-Stokes equations. The space-time mesh is the tensor product of an unstructured spatial mesh and time-slabs. Both the spatial mesh and the set of time-slabs can be refined locally, maintaining the tensor product structure of the space-time mesh. The refinement decision is based on the solution of an adjoint problem and requires storing the solution on all time-slabs, which is infeasible for long running simulations.

In this paper we use a structured coarse space-time mesh, divided into time-slabs, and allow per coarse element a structured refinement. This scheme can easily be extended to multiple levels of refinement in both space and time. Per element the decision to refine is based on a smoothness indicator. Spurious oscillations in the neighbourhood of discontinuities are suppressed by adding artificial viscosity to the model (Persson and Peraire, 2006; Barter and Darmofal, 2010).

The outline of this paper is as follows. In section 2 we recall the governing equations of the compressible two-fluid model, and introduce a new term associated with the hydrostatic pressure variation which is generally neglected in the literature. In section 3 the new *h*-adaptive DGFEM discretisation for the compressible two-fluid model is introduced. In section 4 a common Finite Volume discretisation of the same compressible two-fluid model is given, which will be used to assess the performance of the new DGFEM. In Section 5 we analyse the stability of the two-fluid model and the DGFEM discretisation. Section 6 shows the results for two representative test cases.

2 Governing equations of the compressible two-fluid model

We employ two different one-dimensional models for the simulation of two-phase flow. We label the two phases with G for gas and L for liquid, but the following
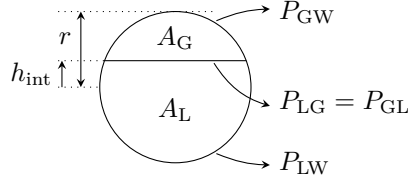
Figure 1: Illustration of phase areas and perimeters as used in the two-fluid model

also applies to a lighter liquid and a heavier liquid. For both models we assume that at least one phase is compressible.

2.1 Two-fluid model

The first, and most general, of the two models is a two-fluid model for stratified flow in a straight, round pipe. Each phase is represented by a mass and momentum balance equation, respectively given by

$$\partial_t \left(A_\beta \rho_\beta \right) + \partial_s \left(A_\beta \rho_\beta u_\beta \right) = 0, \tag{1}$$

and

$$\partial_t \left(A_\beta \rho_\beta u_\beta \right) + \partial_s \left(A_\beta \rho_\beta u_\beta^2 + A_\beta p_{\text{av},\beta} - A_\beta p_{\text{int}} \right) + A_\beta \partial_s p_{\text{int}}$$
$$- \sum_{\substack{\gamma \in \{\text{L,G,W}\} \\ \gamma \neq \beta}} \tau_{\beta\gamma} P_{\beta\gamma} = -A_\beta \rho_\beta g \sin \phi, \tag{2}$$

where $\beta \in \{\text{L}, \text{G}\}$ denotes a phase, t [s] is time, s [m] is the pipe longitudinal distance, ρ_β [kg m^{-3}] is the density of phase β, u_β [m s^{-1}] is the average velocity of phase β in longitudinal direction, A_β [m^2] is the area occupied by phase β and $P_{\beta\gamma}$ [m] is the length of the interface of phase β with $\gamma \in \{\text{L}, \text{G}, \text{W}\}$, where W denotes the pipe wall, $p_{\text{av},\beta}$ [Pa] is the average pressure of phase β, p_{int} [Pa] is the pressure at the interface, h_{int} [m] is the height of the interface with respect to the centre of the pipe, r [m] is the radius of the pipe, g [m s^{-2}] is the gravitational acceleration, ϕ is the angle of the pipe with respect to the horizontal (positive when upward inclined) and $\tau_{\beta\gamma}$ [N m^{-2}] is the average interface friction force between phase β and phase or wall γ. For an illustration of some quantities, see Figure 1.

The model is the result of applying cross-sectional averaging per phase of the three-dimensional conservation of mass and the Navier-Stokes equations. See A for the derivation and for the definition of the phase areas A_β and perimeters $P_{\beta\gamma}$ in terms of the interface height h_{int} and the pipe radius r [m] and the hydrostatic pressure term $p_{\text{av},\beta}$. The model is similar to the models used by Liao et al. (2008) and Fullmer et al. (2014). A difference worth noting is the hydrostatic pressure term $p_{\text{av},\beta}$ in the momentum equation (2), which is present due to the compressibility of the phases.

The shear stress term $\tau_{\beta\gamma}, \beta \in \{\text{G}, \text{L}\}$ is physically modelled by the correlations of Taitel and Dukler (1976):

$$\tau_{\beta\gamma} = \begin{cases} \frac{1}{2} f_\beta \rho_\beta u_\beta \left| u_\beta \right| & \text{if } \gamma = \text{W} \\ \frac{1}{2} f_{\text{int}} \rho_{\text{G}} \left(u_\beta - u_\gamma \right) \left| u_\beta - u_\gamma \right| & \text{if } \gamma \in \{\text{G}, \text{L}\}, \end{cases} \tag{3}$$

6

where μ_β [Pa s] is the dynamic viscosity of phase β, the friction factor f at the phase-wall interfaces and the gas-liquid interface are respectively given by

$$f_\beta = 0.046 \left(\frac{|u_\beta| D_\beta}{\nu_\beta} \right)^{0.2}, \quad \beta \in \{\mathrm{L}, \mathrm{G}\}, \tag{4}$$

and

$$f_{\mathrm{int}} = \max\{f_\mathrm{G}, 0.014\}, \tag{5}$$

and the hydraulic diameters D_β are given by

$$D_\beta = \begin{cases} \frac{4A_\mathrm{L}}{P_\mathrm{LW}} & \text{if } \beta = \mathrm{L}, \\ \frac{4A_\mathrm{G}}{P_\mathrm{GW} + P_\mathrm{GL}} & \text{if } \beta = \mathrm{G}. \end{cases} \tag{6}$$

The two-fluid model is closed by adding the relations which are test case specific, namely the equations of state for the density and viscosity for both phases.

2.2 Homogeneous equilibrium model

The second model considered is the homogeneous equilibrium model. That model is based on the assumption that the two phases are mixed and flow with a single mixture velocity, u_M [m s^{-1}], having a mixture density ρ_M [kg m^{-3}]. The corresponding mass balance equations will then read:

$$\partial_t \left(A_\beta \rho_M \right) + \partial_s \left(A_\beta \rho_M u_M \right) = 0. \tag{7}$$

Compared to the two-fluid model only one, total momentum balance equation remains:

$$\partial_t \left(A_\mathrm{M} \rho_\mathrm{M} u_\mathrm{M} \right) + \partial_s \left(A_\mathrm{M} \rho_\mathrm{M} u_\mathrm{M}^2 + A_\mathrm{M} p_\mathrm{M} \right) = -\tau_\mathrm{MW} P_\mathrm{M} - A_\mathrm{M} \rho_\mathrm{M} g \sin \phi, \tag{8}$$

where τ_MW [N m^{-2}] is the wall friction of the mixture, p_M [Pa] is the average pressure, A_M [m^2] is the area of the pipe cross section,

$$A_\mathrm{M} = A_\mathrm{L} + A_\mathrm{G}, \tag{9}$$

and the mixture density ρ_M [kg m^{-3}] is defined as an area-weighted average of the phase densities,

$$\rho_\mathrm{M} = \frac{A_\mathrm{L} \rho_\mathrm{L} + A_\mathrm{G} \rho_\mathrm{G}}{A_\mathrm{M}}. \tag{10}$$

The total momentum equation (8) *is* conservative, whereas the momentum equations (2) for the two-fluid model are not conservative.

For the wall friction we use Churchill's friction factor. The wall shear stress is given by

$$\tau_\mathrm{MW} = \frac{1}{2} f_\mathrm{MW} \rho_\mathrm{M} u_\mathrm{M} |u_\mathrm{M}|, \tag{11}$$

with friction factor f_MW given by

$$f_\mathrm{MW} = 2 \left(\left(\frac{8}{\mathrm{Re}} \right)^{12} + (\Theta_1 + \Theta_2)^{-1.5} \right)^{\frac{1}{12}}, \tag{12}$$

parameters Θ_1 and Θ_2 given by

$$\Theta_1 = \left(-2.457 \ln \left(\left(\frac{7}{\text{Re}} \right)^{0.9} + 0.27 \frac{\text{pipe roughness}}{2r} \right) \right)^{16}, \qquad (13)$$

and

$$\Theta_2 = \left(\frac{37530}{\text{Re}} \right)^{16}, \qquad (14)$$

The Reynolds number of the mixture is defined as

$$\text{Re} = \frac{2r\rho_{\text{M}}u_{\text{M}}}{\mu_{\text{M}}}, \qquad (15)$$

and the mixture dynamic viscosity is defined as the area-weighted average of the phase viscosities,

$$\mu_{\text{M}} = \frac{A_{\text{L}}\mu_{\text{L}} + A_{\text{G}}\mu_{\text{G}}}{A_{\text{M}}}. \qquad (16)$$

This closes the two-fluid model up to equations of state and viscosity for both phases.

3 Discontinuous Galerkin discretisation of the two-fluid model

In this section we derive the space-time DG discretisation for both models given in Section 2, expressed in general form as

$$\partial_t f_{\text{t}j}(q) + \partial_s f_{\text{s}j}(q) + \sum_k F_{\text{s}jk}(q)\,\partial_s q_k - \partial_s(D_j\partial_s f_{\text{t}j}(q)) + g_j(q) = 0, \quad (17)$$

where $s \in \mathcal{S} \subseteq \mathbb{R}$ refers to space and $t \in \mathcal{T} := [0,T]$ to time, $q : \mathcal{S} \times \mathcal{T} \to \mathbb{R}^N$ is the vector of unknowns as a function of space-time position, $f_{\text{t}} : \mathbb{R}^N \to \mathbb{R}^N$ the mapping from unknowns to conserved quantities, $f_{\text{s}} : \mathbb{R}^N \to \mathbb{R}^N$ the conservative part of the spatial flux, $F_{\text{s}} : \mathbb{R}^N \to \mathbb{R}^{N\times N}$ the non-conservative part of the spatial flux and $g : \mathbb{R}^N \to \mathbb{R}^N$ the source term. For brevity the arguments s and t of q are omitted here and in the following. The diffusion coefficients $D : \mathbb{R}^N$ are introduced for stability and will be discussed in subsection 3.4.

3.1 Weak formulation

Let $(s_a, s_b) \times (t_a, t_b) \subseteq \mathcal{S} \times \mathcal{T}$ be a rectangular space-time element. Let $v : \mathcal{S} \times \mathcal{T} \to \mathbb{R}$ be a function on the space-time domain. Multiplying the general PDE (17) with test function v and integrating over the element gives

$$\int_{s_a}^{s_b} \int_{t_a}^{t_b} v \left(\partial_t f_{\text{t}j}(q) + \partial_s f_{\text{s}j}(q) + \sum_k F_{\text{s}jk}(q)\,\partial_s q_k \right) dt\,ds$$

$$+ \int_{s_a}^{s_b} \int_{t_a}^{t_b} v \left(-\partial_s(D_j\partial_s f_{\text{t}j}(q)) + g_j(q) \right) dt\,ds = 0. \quad (18)$$

Integration by parts of the first, second and fourth term yields

$$\int_{s_a}^{s_b} \int_{t_a}^{t_b} \left(-\partial_t v f_{tj}(q) - \partial_s v f_{sj}(q) + v \sum_k F_{sjk}(q) \partial_s q_k \right) dt \, ds$$

$$+ \int_{s_a}^{s_b} \int_{t_a}^{t_b} \left(\partial_s v D_j \partial_s f_{tj}(q) + v g_j(q) \right) dt \, ds$$

$$+ \left[\int_{s_a}^{s_b} v^{\mathrm{in}} f_{tj}(q^{\mathrm{in}}) \, ds \right]_{t=t_a}^{t_b} + \left[\int_{t_a}^{t_b} v^{\mathrm{in}} f_{sj}(q^{\mathrm{in}}) \, dt \right]_{s=s_a}^{s_b}$$

$$+ \left[\int_{t_a}^{t_b} v^{\mathrm{in}} D_j \partial_s f_{tj}(q^{\mathrm{in}}) \, dt \right]_{s=s_a}^{s_b} = 0. \quad (19)$$

The superscript 'in' denotes the trace of a function from *within* the element, formally

$$q^{\mathrm{in}}(s,t) := \lim_{\epsilon \to 0^+} q\left(s - \epsilon n_s(s,t), t - \epsilon n_t(s,t)\right), \quad (20)$$

with n_s, n_t the unit outward normal of the element. The value at the opposite side of the element boundary is denoted with superscript 'out':

$$q^{\mathrm{out}}(s,t) := \lim_{\epsilon \to 0^+} q\left(s + \epsilon n_s(s,t), t + \epsilon n_t(s,t)\right). \quad (21)$$

3.1.1 Temporal flux

For the temporal flux at the time boundary we use plain upwinding. This amounts to replacing q^{in} in the t_a-boundary integral of Equation (19) with q^{out}. The total time flux boundary contribution becomes

$$\left[\int_{s_a}^{s_b} v^{\mathrm{in}} f_{tj}(q^{\mathrm{in}}) \, ds \right]_{t=t_b} - \left[\int_{s_a}^{s_b} v^{\mathrm{in}} f_{tj}(q^{\mathrm{out}}) \, ds \right]_{t=t_a}, \quad (22)$$

replacing the second term in Equation (19).

3.1.2 Spatial flux

The treatment of the spatial flux at the spatial element boundaries is based on an approximate Riemann solver. Since the system of PDEs is non-conservative, at least for the first model described in Section 2, standard Riemann solvers cannot be applied. Vol'pert (1967) studied non-conservative systems and interpreted the non-conservative product as a product of a function with a measure. Dal Maso et al. (1995) generalised this interpretation of the non-conservative product, known as the *DLM-measure*. At a discontinuity the non-conservative product is defined as the integral of F^{total} over a path connecting both ends of the discontinuity. Given a family of *integration paths*, this gives a rigorous definition of weak solutions to the non-conservative system. Several conservative numerical schemes and approximate Riemann solvers have been generalised to non-conservative systems based on the theory by Dal Maso et al. (1995): Lax-Friedrichs and Lax-Wendroff (Castro et al., 2010), Roe's approximate Riemann solver (Toumi, 1992), HLL (Rhebergen et al., 2008) and the Osher Riemann solver (Dumbser and Toro, 2011). Parés (2006) introduced the concept of path-conservative numerical schemes, as a generalisation of conservative schemes.

Due to the rather complex spatial flux of the two-fluid model defined in Section 2 we did not consider deriving an analytical expression of the eigenvalues and eigenvectors of F^{total}. Instead we rely on numerical computation. Since the Osher Riemann solver (Dumbser and Toro, 2011) requires the eigenstructure to be known along the integration paths connecting both ends of discontinuities, we deemed this method too expensive. The simpler Lax-Friedrichs method is in our experience not stable enough for the PDEs considered in this article. We settled for a linearised Riemann solver based on Roe's approach (Toumi, 1992), which requires a single numerical evaluation of the eigenvalues and eigenvectors per spatial boundary point, but we replace Roe's matrix with $F_{\text{s}}^{\text{total}}(q^{\text{av}})$, where q^{av} is the average value of the inner and outer trace,

$$q_j^{\text{av}} = \frac{1}{2} \left(q_j^{\text{in}} + q_j^{\text{out}} \right), \ \forall j. \tag{23}$$

Let $F_{\text{s}}^{\text{total}} : \mathbb{R}^N \to \mathbb{R}^{N \times N}$ be the total spatial flux matrix, combining the conservative flux Jacobian with the non-conservative flux matrix:

$$F_{\text{s}jl}^{\text{total}} (q) = \partial_{q_l} f_{\text{s}j} (q) + F_{\text{s}jl} (q), \tag{24}$$

and let $F_{\text{s}jl} : \mathbb{R}^N \to \mathbb{R}^{N \times N}$ be the temporal flux Jacobian:

$$F_{\text{t}jl} (q) = \partial_{q_l} f_{\text{t}j} (q). \tag{25}$$

Let λ_k and R_{jk} be the k-th eigenvalue and eigenvector of the generalised eigenvalue problem:

$$\sum_l F_{\text{s}jl}^{\text{total}} (q^{\text{av}}) R_{lk} = \sum_l F_{\text{t}jl} (q^{\text{av}}) R_{jk} \lambda_k \ \forall k. \tag{26}$$

Solving the linearised Riemann problem and selecting the centre state yields

$$q_j^* = q_j^{\text{in}} + \sum_{k,l \text{ if } \lambda_k n_{\text{s}} < 0} R_{jk} R_{kl}^{-1} \left(q_l^{\text{out}} - q_l^{\text{in}} \right). \tag{27}$$

This definition of q^* only applies for internal element boundaries. The domain boundary conditions are described in Section 3.3. Before continuing we need the following definition of integration paths:

Definition 1 (Integration paths, multidimensional version (Dal Maso et al., 1995)) *A Lipschitz continuous path $\phi : [0,1] \times \mathbb{R}^N \times \mathbb{R}^N \to \mathbb{R}^N$ is called an integration path if it satisfies the following properties:*

- *The path defined by states q^- and q^+ begins and ends in those states respectively:*

$$\phi_j \left(0; q^-, q^+ \right) = q_j^- \text{ and } \phi_j \left(1; q^-, q^+ \right) = q_j^+ \ \forall j, \forall q^-, q^+ \in \mathbb{R}^N. \tag{28}$$

- *If both states are equal, the path is constant:*

$$\phi_j \left(\tau; q, q \right) = q_j \ \forall j, \forall q \in \mathbb{R}^N, \tau \in [0,1]. \tag{29}$$

- *For every bounded set $\mathcal{U}$ of $\mathbb{R}^N$, there exists $k \geq 1$ such that*

$$\left| \partial_\tau \phi \left(\tau; q^-, q^+ \right) - \partial_\tau \phi \left(\tau; w^-, w^+ \right) \right| \leq k \left| \left(q^- - w^- \right) - \left(q^+ - w^+ \right) \right|$$
$$\forall q^-, q^+, w^-, w^+ \in \mathcal{U}, \tau \text{ a.e. } \in [0,1]. \tag{30}$$

- *Reversing the arguments reverses the path:*

$$\phi\left(\tau; q^-, q^+\right) = \phi\left(1 - \tau; q^+, q^-\right) \ \forall q^-, q^+ \in \mathbb{R}^N, \tau \in [0, 1]. \quad (31)$$

Proceeding with Roe's approximate Riemann solver the contribution of the spatial flux flowing inward is given by the following term

$$\left[\int_{t_a}^{t_b} v^{\text{in}} \int_0^1 \sum_k F_{sjk}^{\text{total}}\left(\phi\left(\tau\right)\right) \partial_s \phi_k\left(\tau; q^{\text{in}}, q^*\right) d\tau \, dt\right]_{s=s_a}^{s_b}. \quad (32)$$

By Definition 1 and Equation (24) this can be simplified to

$$\left[\int_{t_a}^{t_b} v^{\text{in}} \left(f_{sj}\left(q^*\right) - f_{sj}\left(q^{\text{in}}\right) + \int_0^1 \sum_k F_{sjk}\left(\phi\left(\tau; q^{\text{in}}, q^*\right)\right) \partial_s \phi_k\left(\tau; q^{\text{in}}, q^*\right) d\tau\right) dt\right]_{s=s_a}^{s_b}.$$
(33)

This term is to be added to the left hand side of Equation (19).

We assume a straight path connecting the states q^{in} and q^*:

$$\phi_j\left(\tau; q^{\text{in}}, q^*\right) := q_j^{\text{in}}\left(1 - \tau\right) + q_j^* \tau. \quad (34)$$

The choice of the integration path affects the solution to the discrete system. However, this will not be studied here further. See Alouges and Merlet (2004) and Chalmers and Lorin (2009) for a discussion on integration paths.

3.1.3 Diffusion

Following the DGFEM formulation of Baumann and Oden (1999) for a convection-diffusion model the last term of Equation (19) is replaced by

$$\left[\int_{t_a}^{t_b} -\frac{1}{2} D_j \partial_s \left(v^{\text{out}} + v^{\text{in}}\right) \left(f_{tj}\left(q^{\text{out}}\right) - f_{tj}\left(q^{\text{in}}\right)\right) dt\right]_{s=s_a}^{s_b}$$
$$+ \left[\int_{t_a}^{t_b} \frac{1}{2} D_j \partial_s \left(f_{tj}\left(q^{\text{out}}\right) + f_{tj}\left(q^{\text{in}}\right)\right) \left(v^{\text{out}} - v^{\text{in}}\right) dt\right]_{s=s_a}^{s_b}. \quad (35)$$

Bassi and Rebay (2002) have compared the stabilisation of the diffusion term from Equation (35) with a more elaborate local DG type treatment (Bassi and Rebay, 2000) and they concluded that the latter is superior with respect to the accuracy on coarse meshes. However, due to the additional computational complexity we have chosen for the simpler option.

11

3.1.4 Result

Combining all additions and replacements defined above, the resulting weak formulation is given by

$$
\int_{s_a}^{s_b} \int_{t_a}^{t_b} \left(-\partial_t v f_{\mathrm{t}j}\left(q\right) - \partial_s v f_{\mathrm{s}j}\left(q\right) + v \sum_k F_{sjk}\left(q\right) \partial_s q_k \right) dt\, ds
$$

$$
+ \int_{s_a}^{s_b} \int_{t_a}^{t_b} \left(-\partial_s v D_j \partial_s f_{\mathrm{t}j}\left(q\right) + v g_j\left(q\right) \right) dt\, ds
$$

$$
+ \left[\int_{s_a}^{s_b} v^{\mathrm{in}} f_{\mathrm{t}j}\left(q^{\mathrm{in}}\right) ds \right]_{t=t_b} - \left[\int_{s_a}^{s_b} v^{\mathrm{in}} f_{\mathrm{t}j}\left(q^{\mathrm{out}}\right) ds \right]_{t=t_a}
$$

$$
+ \left[\int_{t_a}^{t_b} v^{\mathrm{in}} \left(f_{\mathrm{s}j}\left(q^*\right) + \int_0^1 \sum_k F_{sjk}\left(\phi\left(\tau;q^{\mathrm{in}},q^*\right)\right) \partial_s \phi_k\left(\tau;q^{\mathrm{in}},q^*\right) d\tau \right) dt \right]_{s=s_a}^{s_b}
$$

$$
- \left[\int_{t_a}^{t_b} \frac{1}{2} D_j \partial_s \left(v^{\mathrm{out}} + v^{\mathrm{in}} \right) \left(f_{\mathrm{t}j}\left(q^{\mathrm{out}}\right) - f_{\mathrm{t}j}\left(q^{\mathrm{in}}\right) \right) dt \right]_{s=s_a}^{s_b}
$$

$$
+ \left[\int_{t_a}^{t_b} \frac{1}{2} D_j \partial_s \left(f_{\mathrm{t}j}\left(q^{\mathrm{out}}\right) + f_{\mathrm{t}j}\left(q^{\mathrm{in}}\right) \right) \left(v^{\mathrm{out}} - v^{\mathrm{in}} \right) dt \right]_{s=s_a}^{s_b} = 0, \quad (36)
$$

with $\phi(\tau;q^{\mathrm{in}},q^*)$ defined as in Equation (34) and q^* as in Equation (27).

3.2 Mesh and basis

We use a structured partition $\mathcal{E}$ of the space-time domain $\mathcal{S} \times \mathcal{T}$ as (coarse) mesh. For each element $E \in \mathcal{E}$ we define a local basis as a tensor product of one-dimensional Legendre basis functions with maximum order p for space and time, with support limited to element E. The basis $\mathcal{Q}$ is defined as union of all element bases.

Given a space-time mesh $\mathcal{E}$ and basis, solving the complete discrete system at once is in general too expensive and also unnecessary. We create a possibly finite sequence $\{\mathcal{E}_0, \mathcal{E}_1, \mathcal{E}_2, \dots\}$ of subsets of $\mathcal{E}$, such that the sequence is a partition of $\mathcal{E}$ and all elements of $\mathcal{E}_k$ are a subset of time-interval $\mathcal{S} \times [t_k, t_{k_1}]$. Let $\mathcal{Q}_k$ be the subset of basis functions with support on time slab k. Given a sequence of time slabs, we can solve each time slab one after another due to upwinding in time (Section 3.1.1).

3.3 Boundary conditions

For the boundary conditions, if present, we use the same machinery as introduced in Section 3.1.2 for the internal element boundaries. In absence of an outer value q^{out}, the linearisation state q^{av}, introduced in Section 3.1, is chosen equal to the inner value q^{in}.

Assume that there are N_{L} problem specific (external) boundary conditions at the left boundary and N_{R} at the right boundary, respectively given by the following roots

$$
f_{j\mathrm{L}}\left(q^*\right) = 0, \quad j \in \{0, 1, \dots, N_{\mathrm{L}} - 1\}, \quad (37)
$$

and

$$
f_{j\mathrm{R}}\left(q^*\right) = 0, \quad j \in \{0, 1, \dots, N_{\mathrm{R}} - 1\}. \quad (38)
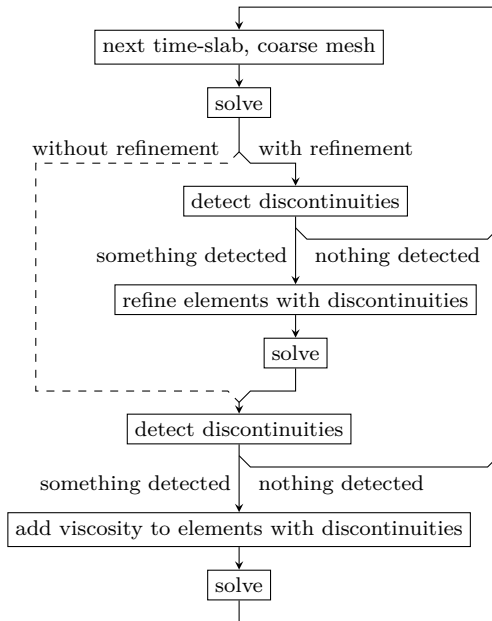$$

Figure 2: DGFEM solver algorithm

These boundary conditions are supplemented with the following (internal) out-flow boundary conditions:

$$\sum_j R_{kj}^{-1} \left(q_j^* - q_j^{\text{in}}\right) = 0 \text{ for all } k \text{ satisfying } \lambda_k n_{\text{s}} > 0, \tag{39}$$

where eigenvalues λ_k and eigenvectors R_{jk} are defined by Equation (26) and n_{s} is the spatial component of the unit outward normal. Note that the number of boundary conditions being the sum of all internal and external conditions, should equal the number of equations n.

3.4 Artificial viscosity

To incorporate artificial viscosity, we use the technique described by Persson and Peraire (2006). For each time-slab we initially solve the system without artificial viscosity. Then we add a fixed amount of viscosity, via parameter D of Equation (17), to all elements for which a smoothness indicator is below a threshold. The algorithm is illustrated in Figure 2.

The smoothness indicator is given by (Persson and Peraire, 2006)

$$\int_{s_a}^{s_b} \int_{t_a}^{t_b} \frac{|q_j - \hat{q}_j|^2}{|q_j|^2} \, dt \, ds, \tag{40}$$

where $\hat{q}$ is equal to the solution q applied with a low pass filter.

3.5 Local refinement

Discontinuities reduce the (uniform) scheme to first order in mesh width. When using a high-order basis, uniform refinement is less effective when discontinuities
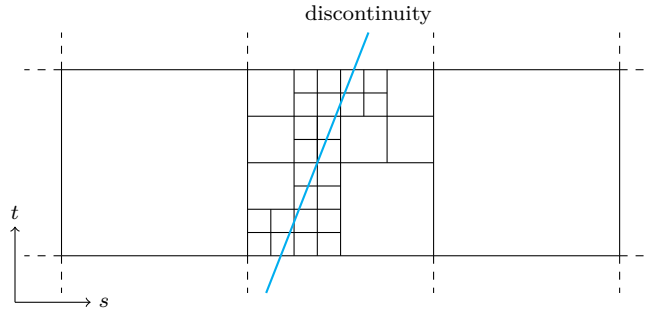
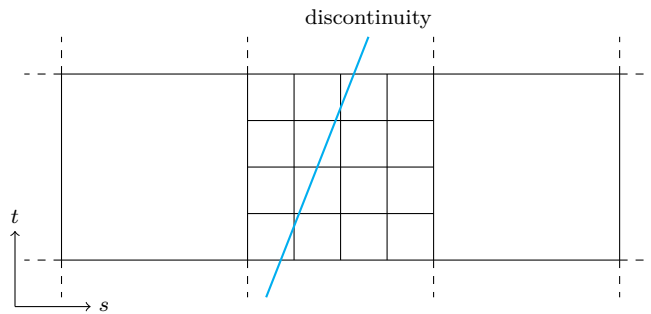Figure 3: Example of multilevel h-refinement near a discontinuity

Figure 4: Example of single-level h-refinement near a discontinuity

are present. To increase the efficiency (in terms of the number of elements in time slab k, $\mathcal{E}_k$, or the number of basis functions in time slab k, $\#\mathcal{Q}_k$) we apply local mesh refinement in the neighbourhood of discontinuities. The most efficient technique would be to gradually refine elements near the discontinuity, as illustrated in Figure 3. As a first step we investigate single-level refinement, where each coarse element can be refined only once, as illustrated in Figure 4.

The procedure is very similar to the addition of artificial viscosity. For each time-slab we compute a solution on a coarse mesh without artificial viscosity. Based on the smoothness indicator we refine elements where the smoothness is below a threshold and recompute a solution on the refined mesh. Finally, we add viscosity to elements with a smoothness below a threshold and recompute a solution one more time. The complete algorithm with refinement and artificial viscosity is illustrated in Figure 2.

4   Finite volume discretisation

4.1   Spatial discretization

We discretise the two-fluid model, i.e. equations (1) and (2), by using a finite volume method on a staggered grid. As indicated in figure 5, the staggered grid consists of both p-volumes, Ω^p, and u-volumes, Ω^u. Each volume consists of a liquid and a gas phase: $\Omega = \Omega_{\mathrm{L}} \cup \Omega_{\mathrm{G}}$, for both u- and p-volumes.
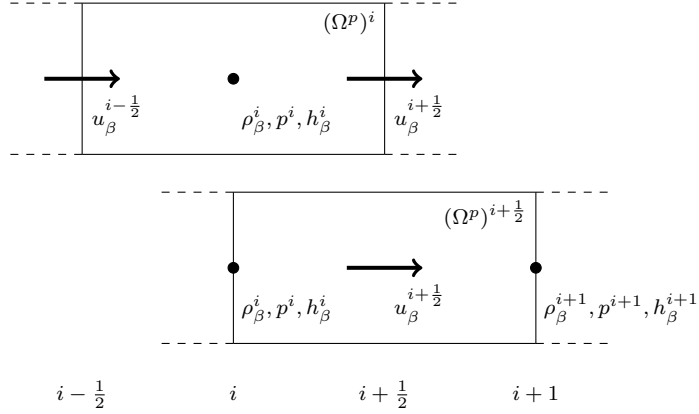
Figure 5: Staggered grid layout of the FV scheme

We start with conservation of mass for a phase β, (β is liquid or gas). Integration of equation (1) in s-direction gives:

$$\partial_t \left(\left(\Omega_\beta^p \right)^i \rho_\beta^i \right) + (A_\beta \rho_\beta)^{i+1/2} u_\beta^{i+1/2} - (A_\beta \rho_\beta)^{i-1/2} u^{i-1/2} = 0, \qquad (41)$$

with the finite volume size approximated by

$$\left(\Omega_\beta^p \right)^i = A_\beta^i \Delta s_p^i. \qquad (42)$$

The finite volume size can be used to rewrite the semi-discrete equation for conservation of mass into:

$$\partial_t \left(A_\beta^i \rho_\beta^i \right) + \frac{(A_\beta \rho_\beta)^{i+1/2} u_\beta^{i+1/2} - (A_\beta \rho_\beta)^{i-1/2} u_\beta^{i-1/2}}{\Delta s_p^i} = 0. \qquad (43)$$

The term $(A_\beta \rho_\beta)^{i+1/2}$ requires interpolation from neighbouring values, which is described below. For conservation of momentum we proceed in a similar way. Integration of (2) in s-direction gives:

$$\begin{aligned}
\partial_t \left(\left(\Omega_\beta^u \right)^{i+1/2} \rho_\beta^{i+1/2} u_\beta^{i+1/2} \right) + (A_\beta \rho_\beta)^{i+1} \left(u_\beta^{i+1} \right)^2 - (A_\beta \rho_\beta)^i \left(u_\beta^i \right)^2 = \\
- A_\beta^{i+1/2} \left(p^{i+1} - p^i \right) - \left(\rho_\beta^{i+1} \mathrm{LG}_\beta^{i+1} - \rho_\beta^i \mathrm{LG}_\beta^i \right) g \cos \phi \\
- \rho_\beta^{i+1/2} g \sin \phi \left(\Omega_\beta^u \right)^{i+1/2} - \sum_{\substack{\gamma \in \{\mathrm{L,G,W}\} \\ \gamma \neq \beta}} \tau_{\beta\gamma}^{i+1/2} P_{\beta\gamma}^{i+1/2} \Delta s_u^{i+1/2}, \quad (44)
\end{aligned}$$

where

$$\left(\Omega_\beta^u \right)^{i+1/2} = A_\beta^{i+1/2} \Delta s_u^{i+1/2}, \qquad (45)$$

and the level gradient terms are given by

$$\mathrm{LG}_\mathrm{G} = h A_\mathrm{G} + \frac{1}{12} w^3, \qquad \mathrm{LG}_\mathrm{L} = h A_\mathrm{L} - \frac{1}{12} w^3. \qquad (46)$$

15

The discretisation of the homogeneous equilibrium model, equations (7) and (8), makes use of the same staggered grid layout. The semi-discrete equations for conservation of mass and momentum for this model will then read:

$$\partial_t \left(A_\beta^i \rho_{\mathrm{M}}^i \right) + \frac{(A_\beta \rho_{\mathrm{M}})^{i+1/2} u_{\mathrm{M}}^{i+1/2} - (A_\beta \rho_{\mathrm{M}})^{i-1/2} u_{\mathrm{M}}^{i-1/2}}{\Delta s_p^i} = 0, \qquad (47)$$

and

$$\begin{aligned}
\partial_t &\left(A_{\mathrm{M}}^{i+1/2} \rho_{\mathrm{M}}^{i+1/2} u_{\mathrm{M}}^{i+1/2} \right) \\
&+ \frac{\left((A_{\mathrm{M}}\rho_{\mathrm{M}})^{i+1} \left(u_{\mathrm{M}}^{i+1}\right)^2 + (A_{\mathrm{M}}p)^{i+1} \right) - \left((A_{\mathrm{M}}\rho_{\mathrm{M}})^i \left(u_{\mathrm{M}}^i\right)^2 + (A_{\mathrm{M}}p)^i \right)}{\Delta s_u^{i+1/2}} \\
&= -\tau_{\mathrm{MW}}^{i+1/2} P_{\mathrm{M}}^{i+1/2} - A_{\mathrm{M}}^{i+1/2} \rho_{\mathrm{M}}^{i+1/2} g \sin \phi. \quad (48)
\end{aligned}$$

Several terms in equations (43), (44) (47) and (48) require approximation. All terms that are not part of the convective terms are interpolated using a central scheme, e.g. $A_\beta^{i+1/2} = \frac{1}{2}(A_\beta^i + A_\beta^{i+1})$. The convective terms, on the other hand, require more care in order to prevent numerical oscillations. They are computed in an upwind fashion using a high resolution scheme as follows. Let ϕ denote a generic quantity on a cell face (either u^2 or ρA) and let θ be a smoothness indicator, given by

$$\theta^{i+1/2} = \frac{\phi_c - \phi_u}{\phi_d - \phi_c}, \qquad (49)$$

where

$$\left. \begin{aligned} \phi_u &= \phi^{i-1} \\ \phi_c &= \phi^i \\ \phi_d &= \phi^{i+1} \end{aligned} \right\} \text{if } u^{i+1/2} \geq 0 \quad , \quad \left. \begin{aligned} \phi_u &= \phi^{i+2} \\ \phi_c &= \phi^{i+1} \\ \phi_d &= \phi^i \end{aligned} \right\} \text{if } u^{i+1/2} < 0, \qquad (50)$$

and ϕ_d, ϕ_u and ϕ_c denote the downstream, upstream and central quantities of the face under consideration. The smoothness indicator is used to compute a slope-limiter $l(\theta)$, from which the face quantity follows as:

$$\phi^{i+1/2} = \phi_c + \frac{1}{2} l^{i+1/2} \left(\phi_d - \phi_c \right). \qquad (51)$$

In the current study the van Albada limiter,

$$l\left(\theta\right) = \frac{\theta^2 + \theta}{\theta^2 + 1}, \qquad (52)$$

has been used, mainly because of its continuous differentiability, which is a favourable property when the fully discrete equations are solved with a Newton solver.

4.2 Boundary conditions

Boundary conditions are set based on the characteristics of the system at the boundary (Olsen, 2004). To determine the characteristic equations, the system is written in quasi-linear form:

$$\partial_t f_{\mathrm{t}j}\left(q\right) + \sum_l F_{sjl}^{\mathrm{total}}\left(q\right) \partial_s q_l + g_j\left(q\right) = 0. \qquad (53)$$

Defining λ_k and R_{jk} as the k-th eigenvalue and eigenvector of $F_{\mathrm{s}jl}^{\mathrm{total}}(q)$, see equation (26), we can write equation (53) as:

$$\partial_t f_{\mathrm{t}j}(q) + \sum_k R_{jk}\ell_k + g_j(q) = 0, \tag{54}$$

where

$$\ell_k = \lambda_k \sum_l R_{kl}^{-1} \partial_s q_l. \tag{55}$$

Equation (54) can now be used for time integration of the boundary points where boundary conditions are set through ℓ_k by making use of the sign of λ_k at the boundary. At the left boundary outgoing waves are associated with negative eigenvalues while at the right boundary outgoing waves are associated with positive eigenvalues. In the case of outgoing waves, equation (55) can be used to calculate ℓ_k by approximating $\partial_s q_l$ with finite differences calculated from the interior of the domain. On the other hand, incoming waves are associated with positive eigenvalues at the left boundary and negative eigenvalues at the right boundary. In the case of incoming waves, ℓ_k can not be calculated from equation (55), rather it is set through the imposed boundary conditions at the left and right boundary. As an example we consider the homogeneous equilibrium model for which we can expect two positive eigenvalues and one negative eigenvalue assuming subsonic flow. This will lead to two incoming waves at the left boundary (inlet), which are determined from the time dependent boundary condition for the mass flow of the gas and the liquid by using equation (54) to solve for ℓ_k. At the right boundary (outlet) we have one incoming wave, which is set by fixing the outlet pressure.

4.3 Temporal discretization

The semi-discrete equations of the two-fluid model (43) and (44) can be written in the form

$$\partial_t f_{\mathrm{t}j}(q) = G_j(q). \tag{56}$$

The semi-discrete equations are solved with the BDF2 scheme (Backward Differentiation Formula):

$$\frac{1}{\Delta t}\left(f_{\mathrm{t}j}\left(q^{n+1}\right) - \frac{4}{3}f_{\mathrm{t}j}\left(q^n\right) + \frac{1}{3}f_{\mathrm{t}j}\left(q^{n-1}\right)\right) = \frac{2}{3}G_j\left(q^{n+1}\right). \tag{57}$$

Equation (57) forms a non-linear system of equations that is solved using a Newton approach:

$$\sum_k \left[\frac{1}{\Delta t}\partial_{q_j}f_{\mathrm{t}k}\left(q^m\right) - \frac{2}{3}\partial_{q_j}G_k\left(q^m\right)\right]\Delta q_k$$
$$= -\left[\frac{1}{\Delta t}\left(f_{\mathrm{t}j}\left(q^m\right) - \frac{4}{3}f_{\mathrm{t}j}\left(q^n\right) + \frac{1}{3}f_{\mathrm{t}j}\left(q^{n-1}\right)\right) - \frac{2}{3}G_j\left(q^m\right)\right]. \tag{58}$$

To solve the non-linear system, we solve for the increments in the primitive variables Δq, but the final system that is solved is (57), and as a consequence mass and momentum will be conserved. The Jacobians $\partial_{q_j}f_{\mathrm{t}k}(q)$ and $\partial_{q_j}G_k(q)$ are computed automatically by using finite differences. The constraint in the form $A_{\mathrm{G}} = A - A_{\mathrm{L}}$ is used to close the system of equations. The time integration of the homogeneous equilibrium model (47) and (48) is done in the same way.

5 Stability and well-posedness

We introduce notions of stability and well-posedness in the general setting of the following quasilinear system of PDEs on infinite spatial domains,

$$\sum_l F_{\mathrm{t}jl}(q)\,\partial_t q_l + \sum_l F_{\mathrm{s}jl}(q)\,\partial_s q_l + g_j(q) = 0, \tag{59}$$

where $q : \mathbb{R} \times [0, T] \to \mathbb{R}^N$ is a vector of quantities, $F_{\mathrm{t}}, F_{\mathrm{s}} : \mathbb{R}^N \to \mathbb{R}^{N \times N}$ are matrices and $g : \mathbb{R}^N \to \mathbb{R}^N$ a vector. For readability the arguments (s, t) of q are omitted. Note that both models introduced in Section 2 can be written in this form. We assume that matrix F_{t} is invertible. However, at the location where one phase is vanishing the two-fluid model given above yields a singular matrix F_{t}. This situation, which occurs when a full liquid slug body is formed, is not considered in this article. Instead we restrict the simulations to the formation and propagation of liquid hold-up waves, which never reach the top of the pipeline.

Assume q is a solution to PDE (59) and constant in space and time. Adding a small perturbation $\epsilon : \mathbb{R} \times [0, T] \to \mathbb{R}^N$ to q and linearising the PDE in ϵ around q yields

$$\sum_l F_{\mathrm{t}jl}(q)\,\partial_t \epsilon_l + \sum_l F_{\mathrm{s}jl}(q)\,\partial_s \epsilon_l + \sum_l \partial_{q_l} g_j(q)\,\epsilon_l = 0. \tag{60}$$

Again, for readability we omit arguments (s, t) of ϵ. Solutions to this linear system of PDEs are of the form

$$\epsilon_j(s, t) = r_j e^{i(ks - \omega t)}, \tag{61}$$

where $r \in \mathbb{C}^N$ is a vector, $k \in \mathbb{R}$ a wave-number and $\omega \in \mathbb{C}$. Substituting the solution (61) into PDE (60), moving the first term to the right hand side and dividing by i yields the following generalised eigenvalue problem with eigenvalue ω and eigenvector r,

$$\sum_l \left(k F_{\mathrm{s}jl}(q) - i\partial_{q_l} g_j(q)\right) r_l = \omega \sum_l F_{\mathrm{t}jl}(q)\,r_l. \tag{62}$$

For a fixed wave-number k all eigenvalues ω and eigenvectors r satisfying this equation define non-trivial solutions to the linearised PDE (60).

Based on the solution (61) we define:

Definition 2 (growth, dissipation) *Growth (in time) is the real part of $-i\omega$, or equivalently the imaginary part of ω. Dissipation is the imaginary part of $-\omega$.*

Definition 3 (dispersion) *Dispersion is the imaginary part of $-i\omega$, or equivalently the real part of $-\omega$.*

The system of PDEs (59) is called *stable* at q if there is no (strictly positive) growth, i.e. for all wave-numbers k all eigenvalues ω of characteristic equation (60) satisfy $\mathrm{Im}\,\omega \le 0$. The system is called *well-posed* if the growth is bounded for all wave-numbers k. An equivalent condition is that all eigenvalues λ of the following generalised eigenvalue problem are real,

$$\sum_l F_{\mathrm{s}jl}(q)\,r_l = \lambda \sum_l F_{\mathrm{t}jl}(q)\,r_l. \tag{63}$$

For models without source terms the notions of well-posedness and stability coincide, i.e. the system is either stable and well-posed or unstable and ill-posed. To see this, note that the characteristic equations (62) and (63) are equivalent, with

$$\lambda = \frac{\omega}{k}, \tag{64}$$

If $\operatorname{Im} \lambda > 0$, then $\operatorname{Im} \omega$ goes to positive infinity for the wave-number k going to infinity, which implies unbounded growth, hence the system is ill-posed.

Both the two-fluid model and the homogeneous equilibrium model have no source terms in case the phases are inviscid and the pipe is horizontal, $\phi = 0$.

5.1 DGFEM

In this section we analyse the effect of the DGFEM scheme on eigenvalue ω.

5.1.1 Spatial

We start with the spatial part of the DGFEM scheme. Multiplying the linearised PDE (62) with a test function, integrating over a spatial element $b \in \mathbb{Z}$ with length Δs, applying integration by parts to the spatial flux term, applying upwinding — see Section 3.1 for the details — and multiplying with the inverse of the mass matrix gives

$$\sum_l F_{\mathrm{t}jl}\left(q\right) \partial_t \hat{\epsilon}_{lmb}$$

$$+ \sum_{ln} F_{sjl}\left(q\right) \left(S_{0mn}\hat{\epsilon}_{lnb} + S_{1mn}\hat{\epsilon}_{ln,b+1} + S_{-1,mn}\hat{\epsilon}_{ln,b-1}\right)$$

$$+ \sum_l \partial_{q_l} g_j\left(q\right) \hat{\epsilon}_{lmb} = 0. \tag{65}$$

where $\hat{\epsilon} : \mathbb{R}^+ \to \mathbb{C}^{N \times N \times \mathbb{Z}}$ is the vector of coefficients as a function of time and $S_0, S_1, S_{-1} \in \mathbb{R}^{(p+1) \times (p+1)}$ are the matrices representing the spatial derivative and upwinding, respectively for element b and the right and left neighbour. Solutions take the form

$$\hat{\epsilon}_{lnb}\left(t\right) = \hat{r}_{ln}\left(t\right) e^{i(kb\Delta s - \hat{\omega}t)}, \tag{66}$$

which differs from the solution of the PDE (61) in $\hat{\omega}$. Substituting this in the DGFEM space discretisation gives

$$-i \sum_{ln} \left(\left(S_{0mn} + S_{1mn}e^{ik\Delta s} + S_{-1,mn}e^{-ik\Delta s}\right) F_{sjl}\left(q\right) + \delta_{mn}\partial_{q_l} g_j\left(q\right)\right) \hat{r}_{ln}$$

$$= \hat{\omega} \sum_l F_{\mathrm{t}jl}\left(q\right) \hat{r}_{lm}. \tag{67}$$

Compared with the characteristic equation (62) there are $N(p+1)$ eigenvalues satisfying Equation (67) instead of N. We were unable to prove that eigenvalues $\hat{\omega}$ converge to ω satisfying Equation (62) or to 0. However, Ainsworth (2004) was able to prove convergence of the wave-number for a scalar, multidimensional PDE, assuming the slightly different solution

$$\hat{\epsilon}_{nb}\left(t\right) = \hat{r}_n\left(t\right) e^{i\left(\hat{k}b\Delta s - \omega t\right)}. \tag{68}$$

Theorem 1 (Convergence of wave-numbers (Ainsworth, 2004)) *Dissipation error:*

$$\left| \text{Im} \left(\hat{k} \Delta s \right) - \text{Im} \left(k \Delta s \right) \right| = O \left(\Delta s^{2p+2} \right). \tag{69}$$

Dispersion error:

$$\left| \text{Re} \left(\hat{k} \Delta s \right) - \text{Re} \left(k \Delta s \right) \right| = O \left(\Delta s^{2p+3} \right). \tag{70}$$

Based on these results and the numerical results in Section 6.1 we conjecture that the two convergence results of Ainsworth (2004) translate to our problem as:

Conjecture 1 (Convergence of eigenvalues) *Eigenvalues $\hat{\omega}$ satisfying characteristic equation (67) converge to ω, the imaginary part with*

$$\left| \text{Im} \left(\hat{k} \Delta s \right) - \text{Im} \left(k \Delta s \right) \right| = O \left(\Delta s^{2p+2} \right) \tag{71}$$

and the real part with

$$\left| \text{Re} \left(\hat{k} \Delta s \right) - \text{Re} \left(k \Delta s \right) \right| = O \left(\Delta s^{2p+3} \right). \tag{72}$$

5.1.2 Temporal

For the analysis of the temporal part we continue with the evolution of a single characteristic wave with eigenvalue $\hat{\omega}$ of the spatial part,

$$\partial_t w \left(t \right) = -i \hat{\omega} w \left(t \right), \tag{73}$$

which admits the following solution:

$$w \left(t \right) = w \left(0 \right) e^{-i \hat{\omega} t}, \quad t > 0. \tag{74}$$

Multiplying this equation with a test function, integrating over temporal element b with length Δt and multiplying with the inverse of the mass matrix yields

$$\sum_m T_{lm,0} \tilde{w}_{mb} + \sum_m T_{lm,-1} \tilde{w}_{m,b-1} = -i \hat{\omega} \tilde{w}_{lb}, \tag{75}$$

where $\tilde{w}_b \in \mathbb{C}^{p+1}$ is the vector of coefficients representing w in element b and matrices $T_{lm,0}, T_{lm,-1} \in \mathbb{R}^{(p+1) \times (p+1)}$ represent the time derivative, acting respectively on the solution of element b and the previous element. Moving the first term to the right hand side and multiplying the equation with the inverse of

$$M_{lm} := T_{lm0} + i \hat{\omega} \delta_{lm} \tag{76}$$

gives

$$\tilde{w}_{jb} = \sum_{lm} M_{jl}^{-1} T_{lm,-1} \tilde{w}_{m,b-1}. \tag{77}$$

Since the solution at element b depends only on the solution at the downwind end of the previous element we can restrict the discrete evolution equation (77) to downwind ends. Let $R \in \mathbb{R}^{p+1}$ be the restriction of a coefficient vector $\tilde{w}$

to downwind ends and $E \in \mathbb{R}^{p+1}$ any expansion of value to a coefficient vector such that the restriction of the expansion is one,

$$\sum_l R_l E_l = 1. \tag{78}$$

Multiplying Equation (77) with R and replacing $\tilde{w}_b$ with the expansion of a scalar $\breve{w} \in \mathbb{C}$ gives the scalar equation

$$\breve{w}_b = G(\hat{\omega}, \Delta t)\, \breve{w}_{b-1} = -\sum_{lm} R_j M_{jl}^{-1} T_{lm} E_m \breve{w}_{b-1}. \tag{79}$$

Lesaint and Raviart (1974) have analysed this DGFEM scheme and proved the following convergence theorem:

Theorem 2 (Convergence of downwind end values (Lesaint and Raviart, 1974)) *The DGFEM scheme (75) converges globally with order $2p + 1$ in time step size Δt, i.e. the error after one step is*

$$\left| G(\hat{\omega}, \Delta t) - e^{-i\hat{\omega}\Delta t} \right| = O\left(\Delta t^{2p+2} \right). \tag{80}$$

This gives the following convergence result for the eigenvalues of the discrete system:

Corollary 1 (Convergence of eigenvalues of discrete system)

$$\left| \breve{\omega} - \hat{\omega} \right| = O\left(\Delta t^{2p+1} \right) \tag{81}$$

Furthermore, Lesaint and Raviart (1974) showed that the DGFEM scheme is strongly A-stable, or L-stable.

6 Results

We analyse the proposed DGFEM scheme using two test cases. In Section 6.1 we present a Kelvin-Helmholtz test case and verify the theoretical stability results presented in Section 5.1. This test case refers to the wave formation at the interface of the flow of air and water in a horizontal pipe at atmospheric pressure. In Section 6.2 we analyse the performance of the DGFEM scheme with and without adaptive refinement.

6.1 Kelvin-Helmholtz

In this section we verify the theoretical results of Section 5 for the two-fluid model discretised with the DG and FV schemes by comparing the theoretical and observed growth rate and dispersion of small sinusoidal waves on infinite domains.

As initial condition we use a constant reference state $q_{\mathrm{ref}} \in \mathbb{R}^N$ that satisfies the system of PDEs with a sinusoidal perturbation with magnitude c,

$$q_{\mathrm{initial},j}(s) = q_{\mathrm{ref},j} + c\,\mathrm{Re}\left(r_j e^{iks} \right), \tag{82}$$

where $r \in \mathbb{R}^N$ is a unit eigenvector of the system linearised around q_{ref}, see Equation (60), and k is a wave-number. As a reference solution we use the exact solution to the linearised model, given by

$$q_{\text{lin},j}\left(s,t\right) = q_{\text{ref},j} + c\,\text{Re}\left(r_j e^{i(ks-\omega t)}\right),\tag{83}$$

where $\omega \in \mathbb{C}$ is the eigenvalue corresponding to the eigenvector r. This is close to the real solution when the amplitude c is very small.

We start the analysis of the uniform DG and FV schemes with the inviscid two-fluid model. We use the following reference state,

$$q_{\text{ref}} = \left[\begin{array}{c} p_{\text{int}} \\ h_{\text{int}} \\ u_{\text{L}} \\ u_{\text{G}} \end{array}\right] = \left[\begin{array}{c} 10^5 \text{ Pa} \\ 0 \text{ m} \\ 1 \text{ m s}^{-1} \\ 15 \text{ m s}^{-1} \end{array}\right],\tag{84}$$

and the following model parameters: pipe radius $r = 0.39$ m, gas density $\rho_{\text{G}} = 1.1614 \cdot 10^{-5} p$ in kg m^{-3}, liquid density $\rho_{\text{L}} = 1000$ kg m^{-3}, gravitational acceleration $g = 9.8$ m s^{-2}, pipe angle $\phi = 0$ and viscosity is set to zero. Note that any choice for the reference state q_{ref} would be an equilibrium solution of the two-fluid model, because the source terms, friction and longitudinal gravity forces, are absent. Since there is no viscosity, the model is either stable and well-posed or unstable and ill-posed. In this case the chosen reference state is in the stable region, but close to the ill-posed region.

We choose $k = 1$ and let ω and r be the third (algebraically) eigenvalue and eigenvector of the system linearised around q_{ref}:

$$\omega = 8.070\ldots \cdot 10^0,\tag{85}$$

and

$$r = \left[\begin{array}{c} -9.980\ldots \cdot 10^{-1} \\ 1.394\ldots \cdot 10^{-4} \\ 1.294\ldots \cdot 10^{-3} \\ 6.255\ldots \cdot 10^{-2} \end{array}\right].\tag{86}$$

Trailing dots indicate that the displayed value is rounded. The amplitude of the perturbation c is chosen such that the amplitude of the liquid holdup perturbation is 10^{-10} for DG and 10^{-6} for FV. We use a smaller perturbation for DG and quad precision arithmetic because for the high-order DG scheme we would not able to observe the expected rate of convergence otherwise. In absence of friction the imaginary part of ω is zero, hence the amplitude of the perturbation should remain constant.

Let the relative error be the L_2-norm of the difference between the discrete solution and the reference solution divided by the L_2-norm of the reference solution. For FV we use the l_2-norm instead of the L_2-norm. Figure 6 shows the relative error of the liquid holdup at $t = 1$, obtained using the second order FV scheme and the DG scheme with bases of order p, i.e. $(p+1)^2$ basis functions per element. The horizontal axis shows the average space-time density of the number of degrees of freedom (dofs) required to represent the discrete solution on the space-time domain $[0,1] \times [0,1]$. For both schemes we set $\Delta t = \Delta s$. Reducing the element width Δs with a factor one half increases the number of dofs by a factor four. A second order scheme theoretically reaches second order

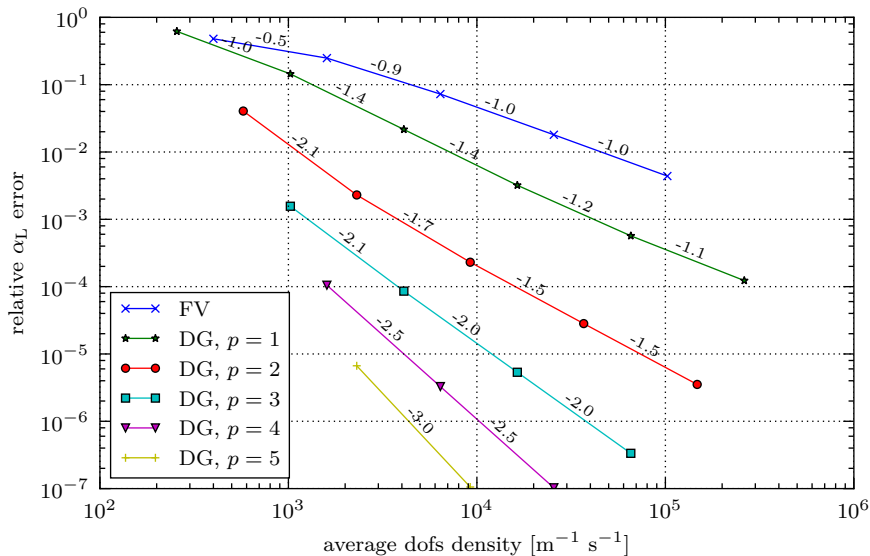Figure 6: Convergence of the relative error of the liquid holdup for the linear, inviscid Kelvin-Helmholtz test-case

convergence with respect to Δs, hence order -1 in terms of dofs. We chose dofs as measure over Δs because the latter is not uniquely defined for non-uniform meshes. All schemes converge with the theoretical rate.

As noted above we are interested in the rate of convergence of the observed eigenvalue of the discrete system. Let q_h be the discrete solution and $\alpha_L(q_h)$ the liquid holdup of the discrete solution. For DG the observed eigenvalue ω_h can be computed by measuring the ratio between the projections of $\alpha_L(q_h)$ on the sinus e^{iks} at time t and 0:

$$\omega_h(t) = \frac{i}{t} \ln \left(\frac{\int_0^{\frac{2\pi}{k}} \alpha_L(q_h(s,t)) e^{-iks} \, ds}{\int_0^{\frac{2\pi}{k}} \alpha_L(q_h(s,0)) e^{-iks} \, ds} \right). \tag{87}$$

We deliberately leave out the projection error, hence the term $q_h(s,0)$ in the denominator instead of $q_{\text{initial}}(s)$. Similarly for FV the observed eigenvalue ω_h is given by

$$\omega_h(t) = \frac{i}{t} \ln \left(\frac{\sum_{l=0}^{n-1} \alpha_L(q_h(s_l,t)) e^{-iks_l} \, ds}{\sum_{l=0}^{n-1} \alpha_L(q_h(s_l,0)) e^{-iks_l} \, ds} \right), \tag{88}$$

where n is the number of cells.

Figure 7 shows the relative error of the growth rate (see Definition 2) at $t = 1$ s. For all DG schemes the growth rate converges with order $-p - 0.5$ with respect to dofs, or $2p + 1$ with respect to the element width Δs. That is significantly faster than the rate with which the discrete solution converges. The convergence rate supports Corollary 1 and is in line with the remainder of the theoretical analysis in Section 5.1. For the FV scheme, however, the amplitude converges at a rate of -1 with respect to dofs, which is the same rate as found for the discrete solution. Similarly, Figure 8 shows the dispersion error (see Defintion 3) at $t = 1$. For the DG schemes the dispersion converges

23
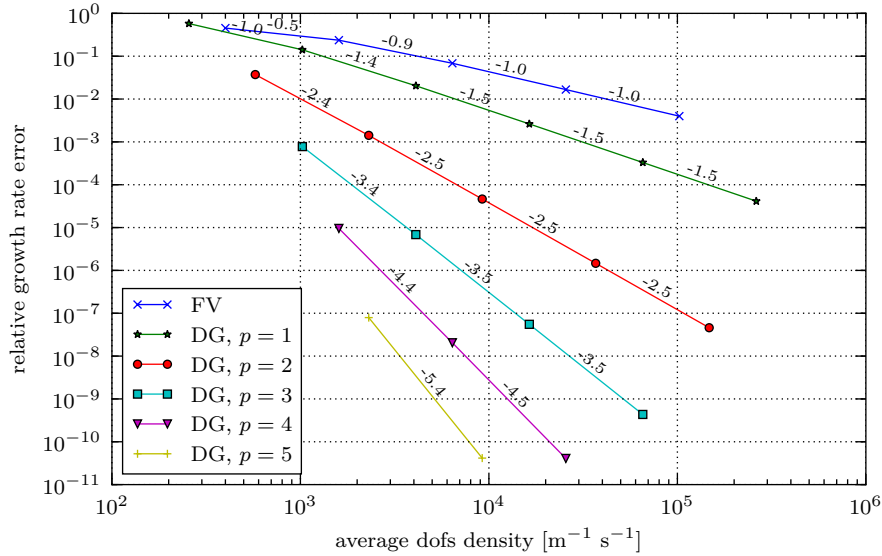
Figure 7: Convergence of the relative error of the growth rate at $t = 1$ s for the linear, inviscid Kelvin-Helmholtz test-case

even faster, with rate $-p-1$, which matches with the theoretical analysis of the spatial part of the DG scheme, but it is better than the theoretical value for the temporal part. Regarding the growth rate and dispersion the superconverging DG scheme outperforms the FV.

Next, we add viscosity to the model and reiterate the above convergence results. The gas dynamic viscosity is set to $\mu_{\mathrm{G}} = 1.8 \cdot 10^{-5}$ Pa s, the liquid dynamic viscosity to $\mu_{\mathrm{L}} = 8.9 \cdot 10^{-4}$ Pa s. The turbulent wall friction and interfacial stress is represented by the model of Taitel and Dukler as was described in Section 2. We set the reference state to

$$
q_{\mathrm{ref}} = \left[\begin{array}{c} p_{\mathrm{int}} \\ h_{\mathrm{int}} \\ u_{\mathrm{L}} \\ u_{\mathrm{G}} \end{array} \right] = \left[\begin{array}{c} 10^5 \text{ Pa} \\ 0 \text{ m} \\ 1 \text{ m s}^{-1} \\ 13.978\ldots \text{ m s}^{-1} \end{array} \right],
\tag{89}
$$

and add the following artificial body force to the right hand side of both phase momentum equations (2)

$$
(76.396\ldots)\, A_\beta.
\tag{90}
$$

The extra body force makes sure that q_{ref} is an equilibrium solution of the model. Both the gas velocity and artificial body force coefficient are obtained by numerically solving for the equilibrium condition: zero net momentum source per phase.

Again, we use initial condition (82) with ω and r equal to the third (algebraically) eigenvalue and eigenvector, and with the amplitude c such that the amplitude of the liquid holdup perturbation is 10^{-10} for DG and 10^{-6} for FV. The third eigenvalue is given by

$$
\omega = 8.457\ldots \cdot 10^0 - 3.605i \cdot 10^{-1}.
\tag{91}
$$

24
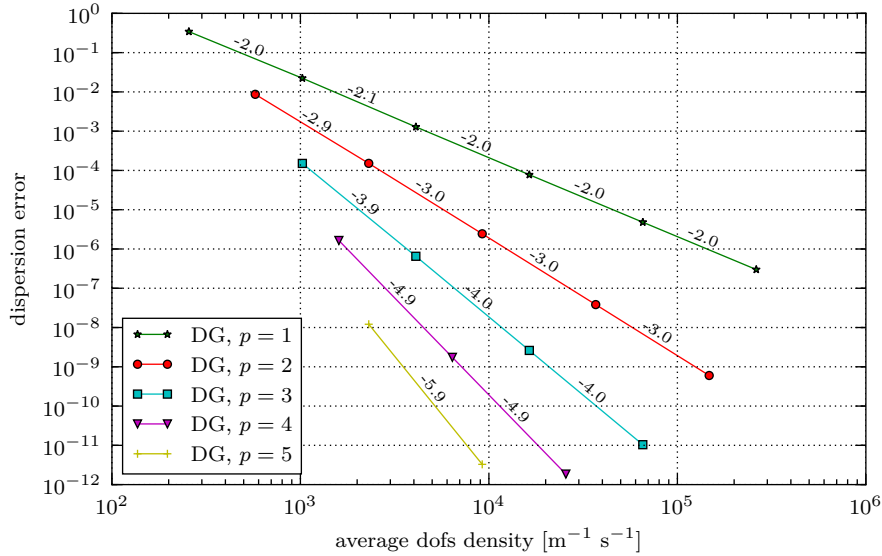
Figure 8: Convergence of the error of the dispersion at $t = 1$ s for the linear, inviscid Kelvin-Helmholtz test-case

and the third eigenvector by

$$
r = \begin{bmatrix}
9.496\ldots \cdot 10^{-1} + 3.062\ldots i \cdot 10^{-1} \\
-1.604\ldots \cdot 10^{-4} - 2.132\ldots i \cdot 10^{-5} \\
-1.852\ldots \cdot 10^{-3} + 5.960\ldots i \cdot 10^{-5} \\
-6.622\ldots \cdot 10^{-2} - 9.132\ldots i \cdot 10^{-3}
\end{bmatrix}
\tag{92}
$$

The eigenvalue has a negative imaginary part, hence the initial perturbation will grow in time.

Figure 9 shows the relative error of the liquid holdup with respect to the exact solution of the linearised model (83). The results are similar to the inviscid case. For the DG schemes the liquid holdup converges with rate $-(p+1)/2$ in terms of dofs. For the FV scheme the rate of convergence is -1. Also the results for the growth rate and dispersion errors, show in Figures 10 and 11, are similar to the inviscid case. The convergence of the dispersion error is now on par with the growth rate error and corresponds to the theoretical analysis of Section 5.1.

We proceed with the same viscous model, but we increase the amplitude c of the initial perturbation such that the amplitude of the liquid holdup perturbation is 10^{-2}. The initial perturbation is now so large that the non-linearity of the model becomes significant. The effect of the non-linearity is visible in Figure 12, which shows the liquid holdup of a discrete solution on part of the spatial domain at time steps $n\omega/k, n \in \{0, 1, \ldots, 6\}$. The sinusoidal perturbation of the liquid holdup grows in time and develops a shock. The third eigenvalue, shown in Figure 13 in the upper half, confirms this: there is a very rapid drop with respect to positive s. The second eigenvalue, shown in the lower half of the same figure, grows towards the third eigenvalue. At the last time step displayed the eigenvalues 'touch' each other and form a pair of complex eigenvalues, which marks the end of the well-posedness of the model.

25
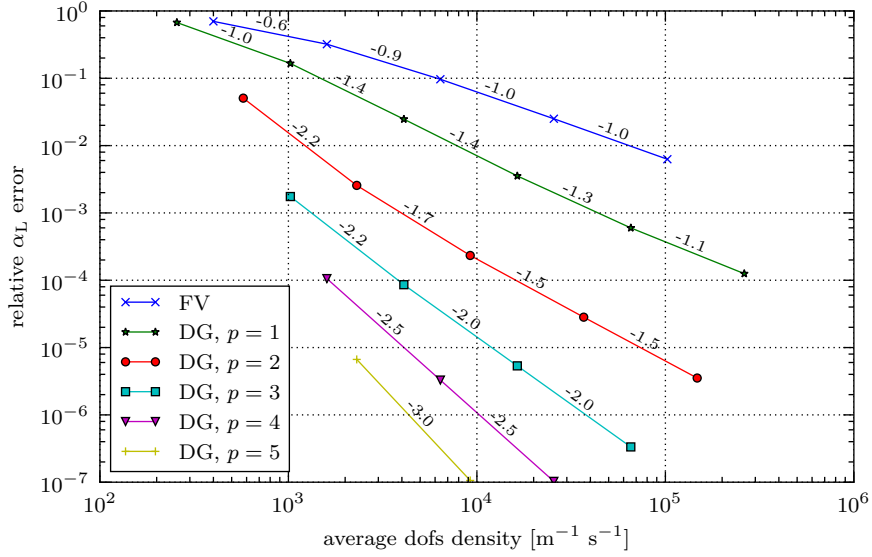
Figure 9: Convergence of the relative error of the liquid holdup for the linear, viscous Kelvin-Helmholtz test-case
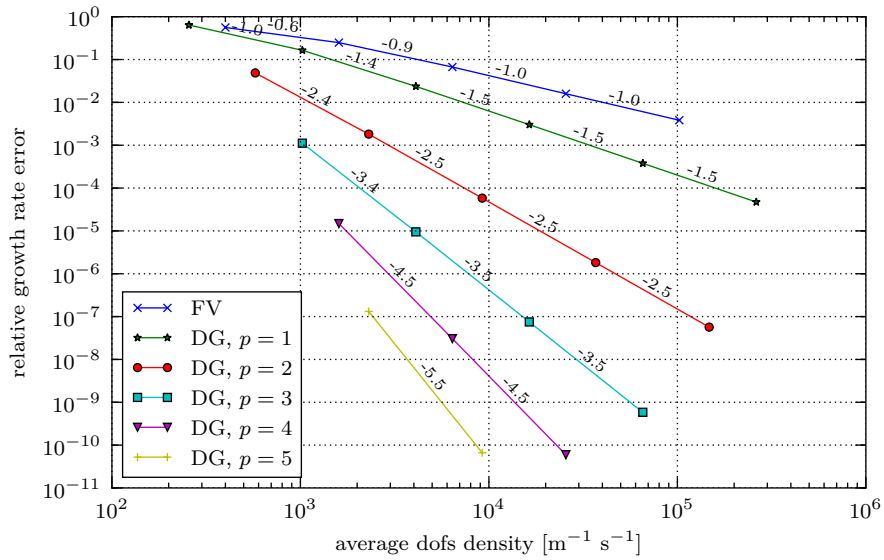

Figure 10: Convergence of the relative amplitude error of the liquid holdup for the linear, viscous Kelvin-Helmholtz test-case
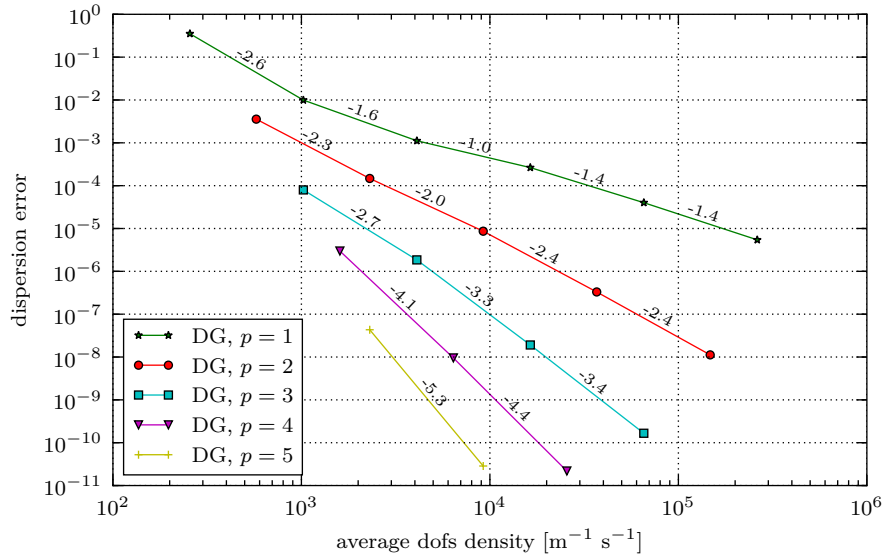
Figure 11: Convergence of the phase shift error of the liquid holdup for the linear, viscous Kelvin-Helmholtz test-case
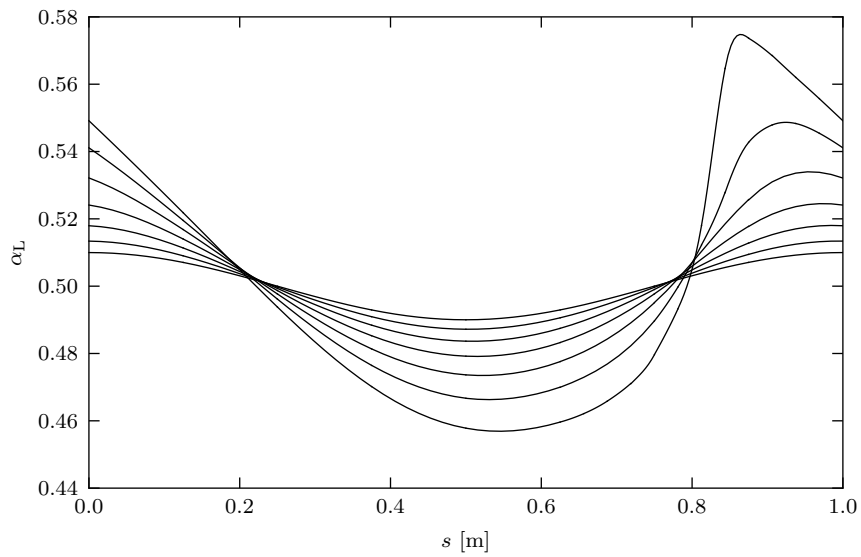

Figure 12: Liquid holdup part of the discrete solution of the non-linear, viscous Kelvin-Helmholtz test case at time steps $t = n\omega/k, n \in \{0, 1, \ldots, 6\}$
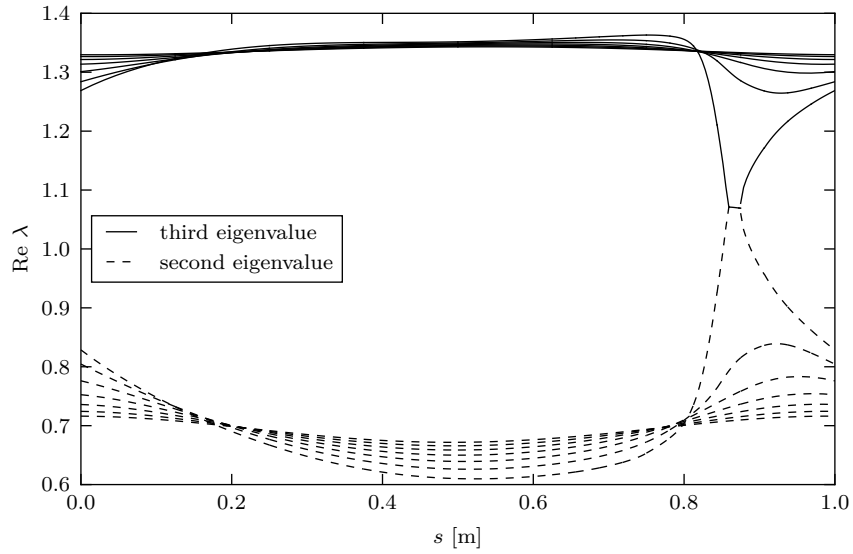
Figure 13: Second and third eigenvalue of the linearised discrete system of the non-linear, viscous Kelvin-Helmholtz test case at time steps $t = n\omega/k, n \in \{0, 1, \ldots, 6\}$
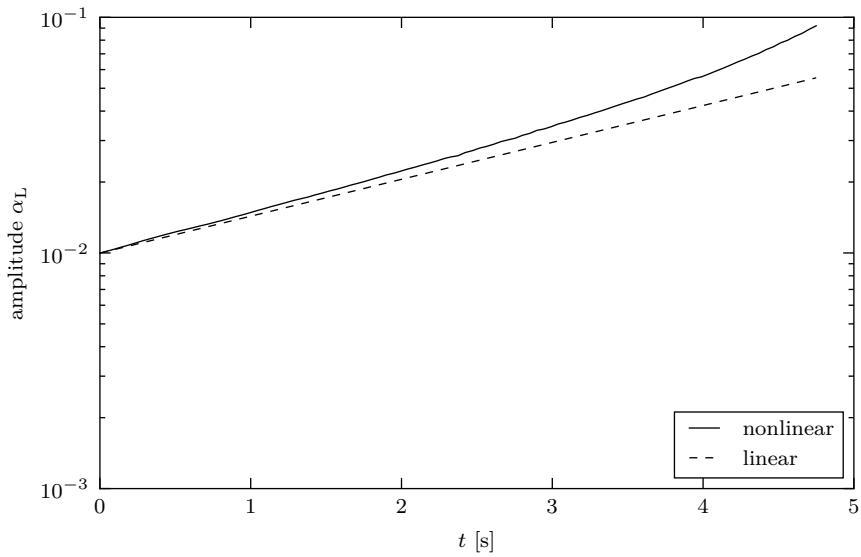
Figure 14: Evolution of the growth of the discrete liquid holdup of the non-linear and linear, viscous Kelvin-Helmholtz test case

6.2 IFP test case

We continue with the IFP test case, proposed by the French Petroleum Institute and described by Omgba-Essama (2004). A 10 km long pipe with a diameter of 0.146 m is fed at the left side with liquid and gas at constant mass flow rates 20 and 0.2 kg s^{-1}, respectively. At the other side the pipe is open at a pressure of 10^6 Pa. At $t = 0$ s the flow is in steady state. Between $t = 0$ and 10 s the gas mass flow rate at the left side changes linearly in time from 0.2 to 0.4 kg s^{-1}. In summary, at the left boundary we have

$$A_\beta \rho_\beta u_\beta = \left\{ \begin{array}{ll} 20 \text{ kg s}^{-1} & \text{if } \beta = \text{L}, \\ 0.2 \text{ kg s}^{-1} & \text{if } \beta = \text{G}, \end{array} \right. \tag{93}$$

and at the right boundary

$$p = 10^6 \text{ Pa}. \tag{94}$$

We use the following equation of state for the gas phase,

$$\rho_\text{G} = 1.26 \frac{p}{10^5} \text{ kg m}^{-3}, \tag{95}$$

and an incompressible water phase with density $\rho_\text{L} = 1003$ kg m^{-3}. The equations of state differ from the original problem definition.

The rapid change in the inlet mass flow rate generates a wave that travels to the other side of the domain. The wave consists of a transition in the liquid holdup over 20 to 30 m and travels with roughly 2 to 3 m s^{-1} through the pipe. After approximately 4500 s the wave has exited the pipe and the flow slowly settles to a new steady state.

6.2.1 Uniform

We use the Homogeneous Equilibrium Model and apply the Finite Volume (FV) scheme and Discontinuous Galerkin (DG) schemes defined earlier to simulate this test case. The ratio between the spatial and the temporal element size, or point distance for FV, is fixed at $16/125$ s m^{-1}, which yields a Courant number of approximately 10. For the DG scheme we use three high-order bases: $p + 1$ number of basis functions per element per dimension, with p ranging from 1 to 3.

Due to the very rapid transition in the liquid holdup and, consequently, short distance over which the liquid holdup changes compared to the length of the pipe, on coarse, uniform meshes the jump is approximately a contact discontinuity. In the FV scheme a limiter is applied to dampen spurious oscillations emanating from this near-discontinuity and in the DG scheme viscosity is added locally, using the approach described in Section 3.4.

Figure 15 shows the relative L_1-error of the liquid holdup at 3600 s for different discretisation schemes. The horizontal axis displays the average number of dofs in space and time. For the Finite Volume and Discontinuous Galerkin schemes with uniform meshes the number of dofs is a quadratic function of the number of spatial grid points or elements, since the ratio of the time step size and the element width, or point distance for FV, is held constant. Doubling the amount of spatial grid points or elements increases the amount of dofs by a factor four.
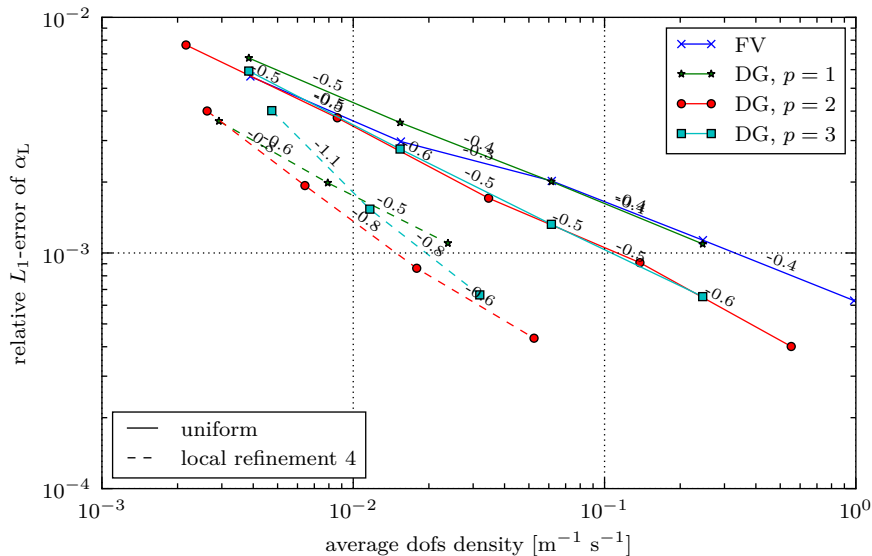
Figure 15: Convergence of the relative L_1-error of the liquid holdup in terms of dofs for the IFP test case at $t = 3600$ s

The FV scheme and DG schemes without local refinement have a comparable performance: all converge roughly with rate -0.5 in terms of dofs. Due to the apparent discontinuity in the liquid holdup the theoretical order of convergence in the L_1-norm is one with respect to the element width, hence -0.5 in terms of dofs. The higher order DG schemes are slightly more accurate than DG with only two basis functions per element per dimension, $p = 1$, for the same number of dofs. However, the computational complexity increases with the number of basis functions per element. To see this we have to look at the time required to compute a solution, displayed for DG in Figure 16. Note that this depends to some extent on the implementation of the numerical schemes and the hardware used to run the simulation. The DG schemes with two and three basis functions per dimension per element, $p = 1$ and $p = 2$, have almost identical performance: the gain in number of dofs for $p = 2$ is lost in the increased computational complexity. The highest order basis considered here, $p = 3$, is slower than $p = 1$ and $p = 2$, despite requiring even fewer dofs than $p = 2$. The rates of convergence in terms of dofs and wall clock time are similar. Solving a time slab requires solving a linear system several times, as part of the Newton linearisation. As the linear system has a fixed bandwidth for fixed number of basis functions, the time required to build and solve the linear system scales linearly with the number of (spatial) elements and the number of dofs. Assuming the number of Newton iterations is independent of the number of elements, the convergence rates in dofs and wall clock time should match. It is important to note that for smooth problems a high-order basis *will* have a higher rate of convergence, both in dofs and wall clock time, outperforming lower order schemes, at least for fine enough meshes.

Figures 17 and 18 show the relative L_1-error of the velocity and pressure at 3600 s versus dofs. Contrary to the liquid holdup there is a significant
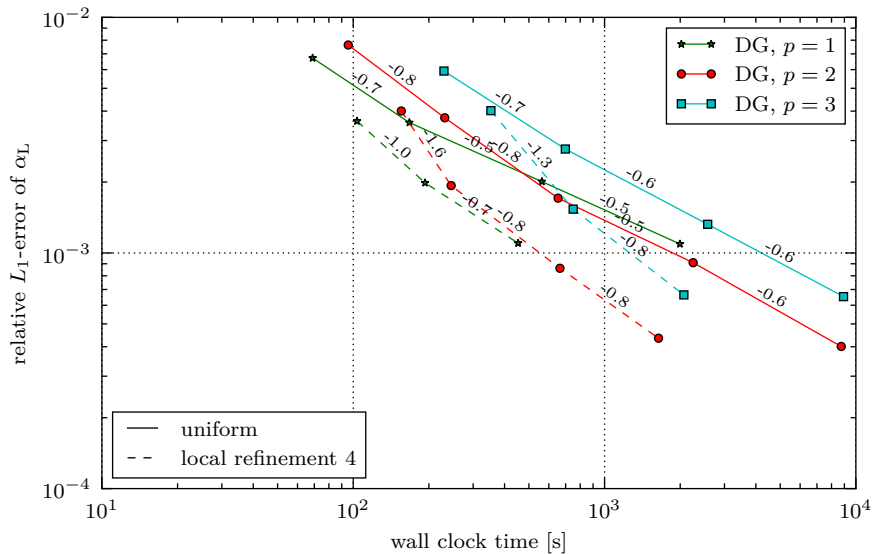
Figure 16: Convergence of the relative L_1-error of the liquid holdup in terms of wall clock time for the IFP test case at $t = 3600$ s

performance difference between the Finite Volume and Discontinuous Galerkin schemes. The FV scheme maintains a convergence rate of roughly -0.5, which is similar to the convergence rate for the liquid holdup. The DG schemes, however, have a higher convergence rate ranging from -0.8 to -1.

6.2.2 Local refinement

To improve the performance we apply local mesh refinement. In the neighbourhood of the discontinuity we subdivide elements equally in four by four parts in space and time and maintain the order of the basis functions.

Figures 19 and 20 show the pointwise error of the liquid holdup and the element density — red indicates a four times refined area — corresponding to a DG scheme with 32 spatial elements and with local refinement near the discontinuity. On average four coarse elements are refined, all near the discontinuity, that is in the region where the pointwise error is large, which shows that the refinement procedure is effective.

Figure 21 shows the pointwise error of the liquid holdup at $t = 3600$ s for uniform meshes with 64 (green dashed) and 256 elements (green dotted) and a coarse mesh of 64 elements with local refinement (red solid), all with $p = 2$. The discontinuity is located approximately at $s = 7500$ m. For all schemes the error is very large near the discontinuity and several orders of magnitude smaller away from the discontinuity. The errors of the fine uniform mesh and the mesh with local refinement are very similar which shows that adding more elements in the smooth region does not improve the accuracy.

The convergence results of applying local refinement are displayed in Figures 15, 16, 17 and 18 as dotted lines, indicated with 'local refinement 4'. Compared to the uniform DG schemes with the same order of basis p, local refinement
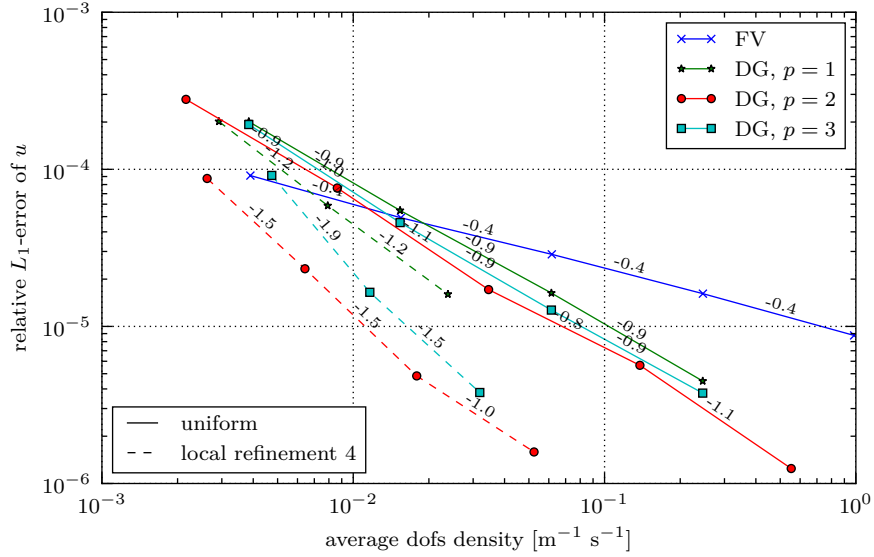
31

Figure 17: Convergence of the relative L_1-error of the velocity in terms of dofs for the IFP test case at $t = 3600$ s
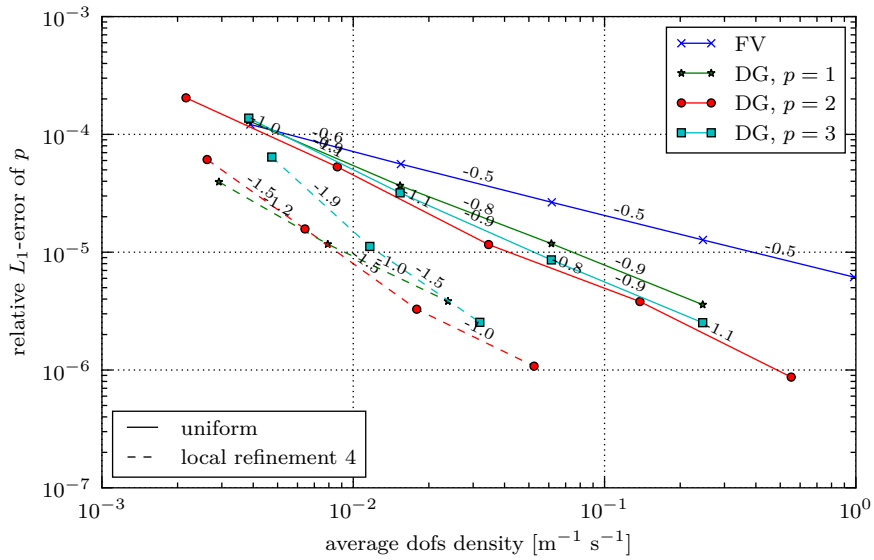

Figure 18: Convergence of the relative L_1-error of the pressure in terms of dofs for the IFP test case at $t = 3600$ s
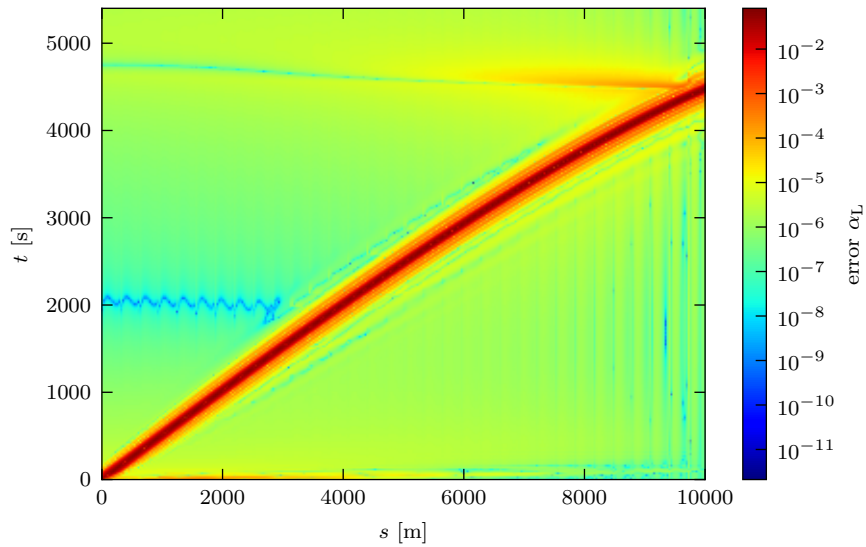
Figure 19: Error of the liquid holdup for the IFP test case with a coarse mesh of 32 spatial elements, a basis of order 2 and adaptive refinement with four by four subdivisions
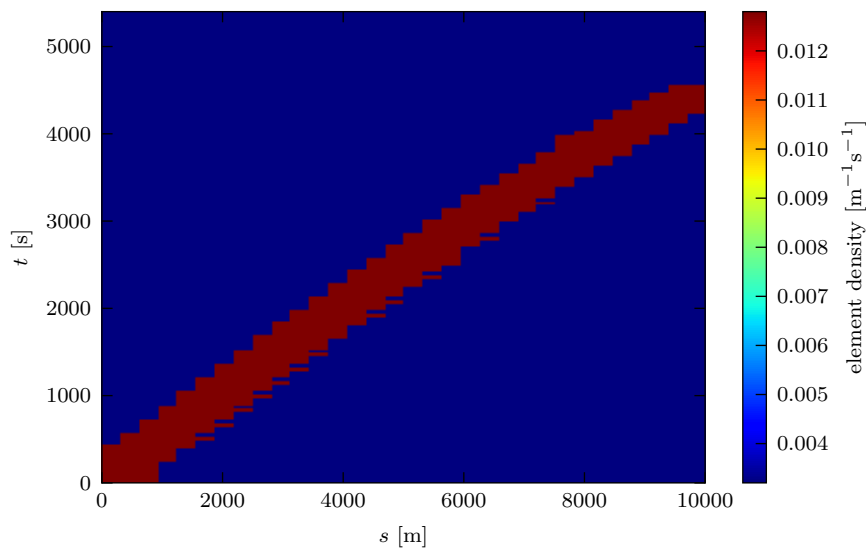

Figure 20: Element density for the IFP test case with a coarse mesh of 32 spatial elements, a basis of order 2 and adaptive refinement with four by four subdivisions
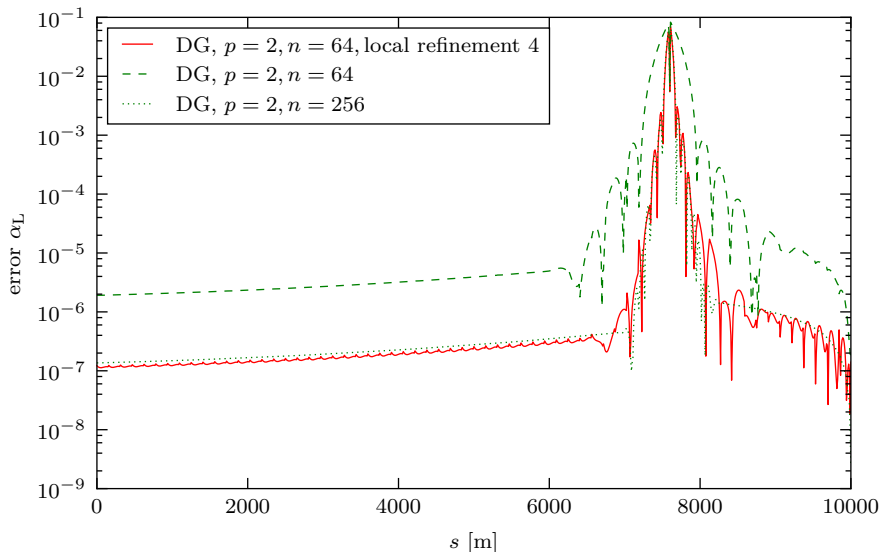
33

Figure 21: Comparison of the error of the liquid holdup for the IFP test case at $t = 3600$ s for uniform schemes with 64 and 256 spatial elements and the adaptive scheme with 64 spatial coarse elements

significantly improves the performance in terms of dofs: the amount of dofs used to represent a solution with a certain accuracy is up to ten times lower.

The rates of convergence of schemes with local refinement tend to the same value as for the uniform schemes. In the neighbourhood of a discontinuity the convergence is at most first order in the *local* mesh width h. Applying a four times refinement in the neighbourhood of a discontinuity does increase the accuracy significantly compared to a uniform coarse mesh, but upon further (coarse) mesh refinement the convergence is again limited to first order in $h/4$. To improve the performance even further, multiple levels of refinement should be applied near the discontinuity.

Figure 22 shows the relative L_1-error in the liquid holdup at 3600 s for the DG scheme with a second order basis for a uniform mesh, and for a mesh with local refinement. The dotted lines connect results obtained with the same coarse mesh, which thus shows the improvement on the relative error when applying local mesh refinement to a certain mesh. The coarsest uniform mesh displayed has 32 elements. Like in the example given earlier the improvement of the error when applying local refinement exceeds -1 in terms of dofs. When increasing the number of elements, the absolute number of elements where refinement occurs stays roughly the same, but the *relative* amount decreases, which increases the rate of convergence.

Refining one element increases the amount of dofs for that element by a factor sixteen and potentially decreases the L_1-error of the liquid holdup by a factor four. If, for example, only four out of 32 elements are refined, the increase in average number of dofs is less than three, giving a potential rate of convergence — going from uniform to locally refined — higher than -1.3 in terms of dofs if the error is dominated by the discontinuity. A four times
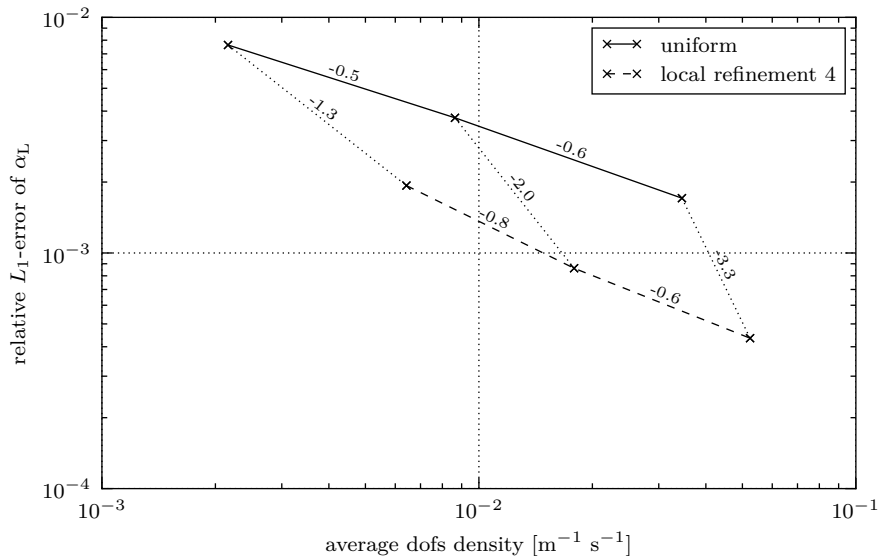
Figure 22: Convergence of the relative L_1-error of the liquid holdup at $t = 3600$ s for DG with $p = 2$ with and without local refinement

uniform refined mesh would require roughly 5.5 times more dofs than with local refinement while having a similar accuracy.

7 Conclusions

We have applied a space-time Discontinuous Galerkin Finite Element Scheme to one-dimensional models for multiphase flow in pipelines and compared the performance with a second order Finite Volume scheme. The solutions of the DGFEM scheme converge in the L_2-norm with the theoretically expected rate of convergence, which is order $p + 1$ in terms of element width, where p is the order of the basis functions. The second order FV scheme shows the expected second order convergence. A linear stability analysis shows that the amplitude and phase shift of a sine wave converge with a higher rate in the DG scheme, being order $2p+1$ in terms of the mesh width, while the second order FV scheme converges only with order 2. This shows that a second order DGFEM scheme is superior to a second order FV scheme, with approximately the same number of dofs.

For problems that develop discontinuities, high-order DGFEM methods suffer from spurious oscillations in the neighbourhood of the discontinuities. To suppress these oscillations we have added an artificial diffusion term to the model. The amount of diffusion is determined by the smoothness of the solution: no diffusion in smooth regions and enough diffusion in irregular regions. Because the diffusion term is PDE-based, no special treatment is required on unstructured meshes.

To increase the efficiency of the DGFEM scheme, we have applied local refinement in both space and time. In case of discontinuities, there is a maximum

rate of convergence of $-1/2$ in terms of dofs for uniform refinement. By refining the mesh in the neighbourhood of discontinuities this limit is surpassed on the global scale. While the refinement scheme requires solving the discrete system twice per time slab, i.e. once on a coarse, uniform mesh and once on the refinement mesh, we have shown that the calculation time for the DGFEM scheme with local refinement is shorter compared to the uniform approach that has the same accuracy.

We recommend investigating multiple levels of refinement to further increase the accuracy in relevant parts of the space-time domain, while keeping the increase in dofs low. Furthermore applying the DGFEM to conditions with a vanishing phase, which gives a singularity, is under investigation.

Acknowledgements

A   Derivation of a two-fluid model

In this section we derive the one-dimensional two-fluid model used in this article. We assume the flow is compressible and stratified in a cylindrical pipe without bends with possibly space- and time-varying radius.

The model follows from averaging for each phase the mass conservation equation

$$\partial_t \rho + \sum_j \partial_{x_j} \left(u_j \rho \right) = 0, \tag{96}$$

and the Navier-Stokes equations

$$\partial_t \left(\rho u_i \right) + \sum_j \partial_{x_j} \left(u_j \rho u_i + p \delta_{ij} - \tau_{ij} \right) = \rho g n_{\text{gravity},j}, \tag{97}$$

over the phase cross sectional area. The model is supplemented by cross sectional pressure variation based on a hydrostatic equilibrium assumption. Friction is usually added using empirical relations, hence τ is set to zero in the following derivation.

A.1   Geometries

We assume the pipe has possibly space- and time-varying radius $r(s,t)$. The frame of reference is chosen as follows: x_0 is the longitudinal direction of the pipe, x_2 the direction orthogonal to the gravity force and x_1 is chosen such that the component of gravity force in this direction is negative. The pipe is elevated with respect to the gravity force with angle ϕ. The direction of the gravity force in the chosen reference frame is given by

$$n_{\text{gravity},j} := \begin{cases} -\sin\phi & j = 0 \\ -\cos\phi & j = 1 \\ 0 & j = 2 \end{cases}. \tag{98}$$

36

The two phases, liquid denoted by subscript L and gas denoted by G, are completely separated: the heavier liquid phase occupies the lower region of the pipe, the lighter gas phase the higher region.

Let $h_{\text{int}}(s,t)$ be the height of the interface between the liquid and gas phase. The liquid and gas phase cross sections are respectively given by

$$\Omega_{\text{L}} := (s,t) \mapsto \{x \in \mathbb{R}^3, x_0 = s, x_1^2 + x_2^2 < r^2(s,t), x_1 < h_{\text{int}}(s,t)\}, \qquad (99)$$

and

$$\Omega_{\text{G}} := (s,t) \mapsto \{x \in \mathbb{R}^3, x_0 = s, x_1^2 + x_2^2 < r^2(s,t), x_1 > h_{\text{int}}(s,t)\}. \qquad (100)$$

The cross section of the pipe is given by

$$\Omega_{\text{pipe}} := (s,t) \mapsto \{x \in \mathbb{R}^3, x_0 = s, x_1^2 + x_2^2 < r^2(s,t)\}. \qquad (101)$$

Let $\Gamma_{\beta\gamma}$ be the interface between phase $\beta \in \{\text{L}, \text{G}\}$ and $\gamma \in \{\text{L}, \text{G}, \text{W}\}$, W denoting the pipe wall:

$$\Gamma_{\beta\gamma} := \begin{cases} \emptyset & \text{if } \gamma = \beta, \\ \partial\Omega_\beta \cap \partial\Omega_{\text{pipe}} & \text{if } \gamma = \text{W}, \\ \partial\Omega_\beta \cap \partial\Omega_\gamma & \text{otherwise.} \end{cases} \qquad (102)$$

The s- and t-velocity of the boundary of the phase cross section Ω_β is given by

$$v_{ki}(x,t) = \begin{cases} \partial_k h(s,t)\,\delta_{i1} & \text{if } x \in \partial\Omega_{\text{L}}(s,t) \cap \partial\Omega_{\text{G}}(s,t), \\ \partial_k r(s,t)\,n_i & \text{if } x \in \partial\Omega_{\text{pipe}}(s,t), \end{cases} \qquad (103)$$

with $k \in \{s,t\}$ and $\beta \in \{\text{L}, \text{G}\}$.

The area of the phase cross sections is given by

$$A_{\text{L}} = r^2 \arccos\left(-\frac{h_{\text{int}}}{r}\right) + h_{\text{int}}\sqrt{r^2 - h_{\text{int}}^2}, \qquad (104)$$

and

$$A_{\text{G}} = r^2 \arccos\left(\frac{h_{\text{int}}}{r}\right) - h_{\text{int}}\sqrt{r^2 - h_{\text{int}}^2}. \qquad (105)$$

The perimeters of the liquid-gas, liquid-wall and gas-wall interfaces are respectively given by

$$P_{\text{LG}} = P_{\text{GL}} = 2\sqrt{r^2 - h_{\text{int}}^2}, \qquad (106)$$

$$P_{\text{LW}} = 2r \arccos\left(-\frac{h_{\text{int}}}{r}\right), \qquad (107)$$

and

$$P_{\text{GW}} = 2r \arccos\left(\frac{h_{\text{int}}}{r}\right). \qquad (108)$$

A.2 Averaging

Each of the conservation laws (96) and (97) can be written in the general form

$$\partial_t q\,(x,t) + \sum_i \partial_{x_i} f_i\,(x,t) = g\,(x,t)\,, \tag{109}$$

where q is the conserved quantity, f_i the flux in direction i and g a source term. Averaging the conservation law over a space- and time-varying subset of a plane in $\mathbb{R}^3$,

$$\Omega\,(s,t) \subset \{x \in \mathbb{R}^3, x_0 = s\}, \tag{110}$$

gives

$$\int_{\Omega(s,t)} \left(\partial_t q\,(x,t) + \sum_i \partial_{x_i} f_i\,(x,t) - g\,(x,t) \right) d\mathcal{H}^2\,(x) = 0, \tag{111}$$

where $\mathcal{H}^n$ is the n dimensional Hausdorff measure of $\mathbb{R}^3$.

Let $v_s(x,t) \in \mathbb{R}^3$ and $v_t(x,t) \in \mathbb{R}^3$ be the s- and t-velocity of the boundary of $\Omega(s,t)$ at x with $x_0 = s$. We use Reynolds' transport theorem to interchange integration and differentiation with respect to t and x_0. For t:

$$\partial_t \int_{\Omega(s,t)} q\,(x,t)\ d\mathcal{H}^2\,(x) = \int_{\Omega(s,t)} \partial_t q\,(x,t)\ d\mathcal{H}^2\,(x)$$
$$+ \int_{\partial\Omega(s,t)} q\,(x,t) \sum_k v_{tk}\,(x,t)\, n_k d\mathcal{H}^1\,(x). \tag{112}$$

For x_0:

$$\partial_s \int_{\Omega(s,t)} f_0\,(x,t)\, d\mathcal{H}^2\,(x) = \int_{\Omega(s,t)} \partial_{x_0} f_0\,(x,t)\ d\mathcal{H}^2\,(x)$$
$$+ \int_{\partial\Omega(s,t)} f_0\,(x,t) \sum_k v_{sk}\,(x,t)\, n_k d\mathcal{H}^1\,(x). \tag{113}$$

We apply integration by parts to the remaining spatial derivatives:

$$\int_{\Omega(s,t)} \sum_{j \neq 0} \partial_{x_j} f_j\,(x,t)\, d\mathcal{H}^2\,(x) = \int_{\partial\Omega(s,t)} \sum_{j \neq 0} f_j\,(x,t)\, n_j\ d\mathcal{H}^1\,(x)$$
$$= \int_{\partial\Omega(s,t)} \sum_j f_j\,(x,t)\, n_j\ d\mathcal{H}^1\,(x). \tag{114}$$

The second identity follows from n_0 being zero.

Applying Equations (112), (113) and (114) to the averaged conservation law (111) yields

$$\partial_t \int_{\Omega(s,t)} q\,(x,t)\ d\mathcal{H}^2\,(x)$$
$$+ \int_{\partial\Omega(s,t)} \sum_j (f_j\,(x,t) - q\,(x,t)\, v_{tj}\,(x,t) - f_0\,(x,t)\, v_{sj}\,(x,t))\, n_j\ d\mathcal{H}^1\,(x)$$
$$+ \partial_s \int_{\Omega(s,t)} f_0\,(x,t)\, d\mathcal{H}^2\,(x) = \int_{\Omega(s,t)} g\,(x,t)\ d\mathcal{H}^2\,(x). \tag{115}$$

A.3 Hydrostatic pressure

We define $p_{\text{int}}(s,t)$ as the pressure at the interface between the liquid and the gas phase. We neglect density variation in the phase cross sections Ω_β and approximate the phase densities using the interface pressure p_{int}. For $x \in \Omega_\beta(s,t)$:

$$\rho(x,t) := \rho_\beta(p_{\text{int}}(s,t)), \tag{116}$$

where $\rho_\beta(p)$ is the equation of state of phase β.

The pressure in the phase cross section Ω_β is approximated by solving the momentum equation in vertical direction x_1, assuming the fluid is at rest.

$$\partial_{x_1} p(x,t) = -\rho(x,t)\, g \cos\phi = -\rho_\beta(p_{\text{int}}(s,t))\, g \cos\phi. \tag{117}$$

Solving this differential equation with the condition

$$p(x,t) = p_{\text{int}}(s,t), \forall x \in \mathbb{R}^3 \text{ such that } x_0 = s \text{ and } x_1 = h_{\text{int}}. \tag{118}$$

yields

$$p(x,t) = p_{\text{int}}(s,t) + \rho_\beta(p_{\text{int}}(s,t))\, g \cos\phi\, (h_{\text{int}}(s,t) - x_1). \tag{119}$$

Let w be the width of the pipe at a certain height:

$$w(h,r) := 2\sqrt{r^2 - h^2}. \tag{120}$$

Integrating the pressure p over a phase cross section Ω_β yields

$$\int_{\Omega_\beta(s,t)} p(x,t)\; d\mathcal{H}^2(x)$$
$$= \int_{-r}^{h_{\text{int}}(s,t)} (p_{\text{int}}(s,t) + \rho_\beta(p_{\text{int}}(s,t))\, g \cos\phi\, (h_{\text{int}}(s,t) - h))\, w(h, r(s,t))\, d\lambda(h). \tag{121}$$

Shifting all h invariant terms out of the integrand yields an integral of $w(h,r)$, which equals A_β, and an integral of $hw(h,r)$:

$$\int_{-r}^{h_{\text{int}}} hw(h,r)\, d\lambda(h) = \int_{-r}^{h_{\text{int}}} 2h\sqrt{r^2 - h^2}\, d\lambda(h) = \int_{r^2}^{h_{\text{int}}^2} \sqrt{r^2 - z}\, d\lambda(z)$$
$$= -\frac{2}{3}\left(r^2 - z\right)^{\frac{3}{2}}\Big]_{z=r^2}^{h_{\text{int}}^2} = -\frac{1}{12} w(h_{\text{int}}, r)^3 \tag{122}$$

Substituting this result in Equation (121) gives the integrated pressure of the liquid phase:

$$A_L p_{\text{av,L}}(s,t) := \int_{\Omega_{\text{L}}(s,t)} p(x,t)\, d\mathcal{H}^2(x) = p_{\text{int}}(s,t)\, A_{\text{L}}(s,t)$$
$$+ \rho_{\text{L}}(p_{\text{int}}(s,t))\, g \cos\phi \left(h_{\text{int}}(s,t)\, A_{\text{L}}(s,t) + \frac{1}{12} w(h_{\text{int}}(s,t), r(s,t))^3 \right) \tag{123}$$

Similarly, for the gas phase:

$$A_G p_{\text{av,G}}(s,t) := \int_{\Omega_{\text{G}}(s,t)} p(x,t)\; d\mathcal{H}^2(x) = p_{\text{int}}(s,t)\, A_{\text{G}}(s,t)$$
$$+ \rho_{\text{G}}(p_{\text{int}}(s,t))\, g \cos\phi \left(h_{\text{int}}(s,t)\, A_{\text{G}}(s,t) - \frac{1}{12} w(h_{\text{int}}(s,t), r(s,t))^3 \right) \tag{124}$$

A.4 One-dimensional model

We define average quantities $\bar{q}(s,t)$ of continuous quantities $q(x,t)$ as

$$\bar{q}_\beta(s,t) := \frac{1}{A_\beta(s,t)} \int_{\Omega_\beta(s,t)} q(x,t)\ d\mathcal{H}^2(x), \qquad (125)$$

and approximate the average of a product of quantities as the product of the averages of the quantities. In the following we drop the bar denoting the averaging.

Summarising the above, the mass balance equations for phase $\beta \in \{L, G\}$ is

$$\partial_t(A_\beta \rho_\beta) + \partial_s(A_\beta \rho_\beta u_\beta) = 0, \qquad (126)$$

the momentum balance equation for the liquid phase is

$$\partial_t(A_L \rho_L u_L) + \partial_s\left(A_L \rho_L u_L^2 + A_L p_{av,L}\right) - p_{int} w(h_{int}, r) \partial_s h_{int}$$
$$= -A_L \rho_L g \sin\phi \quad (127)$$

and the momentum balance equation for the gas phase is

$$\partial_t(A_G \rho_G u_G) + \partial_s\left(A_G \rho_G u_G^2 + A_G p_{av,G}\right) + p_{int} w(h_{int}, r) \partial_s h_{int}$$
$$= -A_G \rho_G g \sin\phi. \quad (128)$$

We add the following empirical friction term

$$- \sum_{\substack{\gamma \in \{L,G,W\} \\ \gamma \neq \beta}} \tau_{\beta\gamma} P_{\beta\gamma} \qquad (129)$$

with to be defined parameter τ to the left hand side of both momentum equations. Using the identities

$$w(h_{int}, r) \partial_s h_{int} = \partial_s A_L = -\partial_s A_G \qquad (130)$$

we can write both momentum balance equations as

$$\partial_t(A_\beta \rho_\beta u_\beta) + \partial_s\left(A_\beta \rho_\beta u_\beta^2 + A_\beta p_{av,\beta} - A_\beta p_{int}\right) + A_\beta \partial_s p_{int}$$
$$- \sum_{\substack{\gamma \in \{L,G,W\} \\ \gamma \neq \beta}} \tau_{\beta\gamma} P_{\beta\gamma} = -A_\beta \rho_\beta g \sin\phi, \quad (131)$$

with A_β given by Equations (104) and (105), ρ_β given by an equation of state using p_{int} as reference pressure, $p_{av,\beta}$ given by Equations (123) and (124),

References

B. H. Stewart, B. Wendroff, Two-phase Flow: Models and Methods, J. Comput. Phys. 56 (3) (1984) 363–409, doi:10.1016/0021-9991(84)90103-7.

M. Ishii, T. Hibiki, Thermo-Fluid Dynamics of Two-Phase Flow, Springer New York, doi:10.1007/978-1-4419-7985-8, 2011.

R. I. Issa, M. H. W. Kempf, Simulation of slug flow in horizontal and nearly horizontal pipes with the two-fluid model, Int. J. Multiph. Flow 29 (1) (2003) 69–95, doi:10.1016/S0301-9322(02)00127-1.

K. H. Bendiksen, D. Malnes, R. Moe, S. Nuland, The Dynamic Two-Fluid Model OLGA: Theory and Application, Tech. Rep. SPE/19451, Institutt for Energiteknikk, 1991.

S. Evje, T. Flåtten, Hybrid Flux-Splitting Schemes for a Common Two-Fluid Model, J. Comput. Phys. 192 (1) (2003) 175–210, doi:10.1016/j.jcp.2003.07.001.

J. Liao, R. Mei, J. Klausner, A study on the numerical stability of the two-fluid model near ill-posedness, Int. J. Multiph. Flow 34 (11) (2008) 1067–1087, doi:10.1016/j.ijmultiphaseflow.2008.02.010.

H. Holmås, Numerical simulation of waves in two-phase pipe flow using 1D two-fluid models, Ph.D. thesis, University of Oslo, 2008.

W. D. Fullmer, V. H. Ransom, M. A. Lopez de Bertodano, Linear and nonlinear analysis of an unstable, but well-posed, one-dimensional two-fluid model for two-phase flow based on the inviscid KelvinHelmholtz instability, Nucl. Eng. Des. 268 (2014) 173–184, doi:10.1016/j.nucengdes.2013.04.043.

W. D. Fullmer, M. A. Lopez de Bertodano, X. Zhang, Verification of a Higher-order Finite Difference Scheme for the One-dimensional Two-fluid Model, The Journal of Computational Multiphase Flows 5 (2) (2013) 139–156, doi:10.1260/1757-482X.5.2.139.

M. Bonizzi, R. I. Issa, On the simulation of three-phase slug flow in nearly horizontal pipes using the multi-fluid model, Int. J. Multiph. Flow 29 (11) (2003) 1719–1747, doi:10.1016/j.ijmultiphaseflow.2003.09.002.

H. Holmås, D. Clamond, H. P. Langtangen, A pseudospectral Fourier method for a 1D incompressible two-fluid model, Int. J. Numer. Meth. Fluids 58 (6) (2008) 639–658, doi:10.1002/fld.1772.

A. Üngör, A. Sheffer, Tent-Pitcher: A meshing algorithm for space-time discontinuous Galerkin methods, in: Proceedings of the 9th international meshing roundtable, url: `https://www.cise.ufl.edu/~ungor/abstracts/imr00.html`, 2000.

R. Abedi, M. A. Hawker, R. B. Haber, K. Matouš, An adaptive spacetime discontinuous Galerkin method for cohesive models of elastodynamic fracture, Int. J. Numer. Meth. Eng. 81 (10) (2010) 1207–1241, doi:10.1002/nme.2723.

G. Gassner, M. Staudenmaier, F. Hindenlang, M. Atak, C.-D. Munz, A space-time adaptive discontinuous Galerkin scheme, Computers & Fluids 117 (2015) 247–261, doi:10.1016/j.compfluid.2015.05.002.

W. E. H. Sollie, O. Bokhove, J. J. W. van der Vegt, Spacetime discontinuous Galerkin finite element method for two-fluid flows, J. Comput. Phys. 230 (3) (2011) 789–817, doi:j.jcp.2010.10.019.

K. J. Fidkowski, Y. Luo, Output-based space-time mesh adaptation for the compressible Navier-Stokes equations, J. Comput. Phys. 230 (14) (2011) 5753–5773, doi:10.1016/j.jcp.2011.03.059.

P. O. Persson, J. Peraire, Sub-Cell Shock Capturing for Discontinuous Galerkin Methods, in: Proceedings of the 44th AIAA Aerospace Sciences Meeting and Exhibit, American Institute of Aeronautics and Astronautics, doi:10.2514/6. 2006-112, 2006.

G. E. Barter, D. L. Darmofal, Shock capturing with PDE-based artificial viscosity for DGFEM: Part I. Formulation, J. Comput. Phys. 229 (5) (2010) 1810–1827, doi:10.1016/j.jcp.2009.11.010.

Y. Taitel, A. E. Dukler, A Model for Predicting Flow Regime Transitions in Horizontal and Near Horizontal Gas-Liquid Flow, AIChE J. 22 (1) (1976) 47–55, doi:10.1002/aic.690220105.

A. I. Vol'pert, The Spaces BV and Quasilinear Equations, Math. USSR-Sbornik 2 (2) (1967) 225–267, doi:10.1070/sm1967v002n02abeh002340.

G. Dal Maso, P. G. LeFloch, F. Murat, Definition and Weak Stability of Nonconservative Products, J. Math. Pures Appl. 74 (6) (1995) 483–548.

M. J. Castro, A. Pardo, C. Parés, E. F. Toro, On Some Fast Well-Balanced First Order Solvers For Nonconservative Systems, Math. Comp. 79 (271) (2010) 1427–1472, doi:10.1090/S0025-5718-09-02317-5.

I. Toumi, A weak formulation of Roe's approximate Riemann solver, J. Comput. Phys. 102 (2) (1992) 360–373, doi:10.1016/0021-9991(92)90378-C.

S. Rhebergen, O. Bokhove, J. J. W. van der Vegt, Discontinuous Galerkin Finite Element Methods for Hyperbolic Nonconservative Partial Differential Equations, J. Comput. Phys. 227 (3) (2008) 1887–1922, doi:10.1016/j.jcp.2007.10. 007.

M. Dumbser, E. F. Toro, A Simple Extension of the Osher Riemann Solver to Non-conservative Hyperbolic Systems, J. Sci. Comput. 48 (1–3) (2011) 70–88, doi:10.1007/s10915-010-9400-3.

C. Parés, Numerical methods for nonconservative hyperbolic systems: a theoretical framework., SIAM J. Numer. Anal. 44 (1) (2006) 300–321, doi: 10.1137/050628052.

F. Alouges, B. Merlet, Approximate Shock Curves for Non-Conservative Hyperbolic Systems in One Space Dimension, J. Hyperbol. Differ. Eq. 1 (4) (2004) 769–788, doi:10.1142/S0219891604000251.

N. Chalmers, E. Lorin, Approximation of Nonconservative Hyperbolic Systems Based on Different Nonconservative Product Definitions, Canadian Appl. Math. Q. 17 (3) (2009) 447–485.

C. E. Baumann, J. T. Oden, A discontinuous hp finite element method for convection-diffusion problems, Comp. Meth. Appl. Mech. Eng. 175 (3–4) (1999) 311–341, doi:10.1016/s0045-7825(98)00359-4.

F. Bassi, S. Rebay, Numerical evaluation of two discontinuous Galerkin methods for the compressible Navier-Stokes equations, Int. J. Numer. Meth. Fluids 40 (1–2) (2002) 197–207, doi:10.1002/fld.338.

F. Bassi, S. Rebay, GMRES Discontinuous Galerkin Solution of the Compressible Navier-Stokes Equations, in: B. Cockburn, G. Karniadakis, C.-W. Shu (Eds.), Discontinuous Galerkin Methods, vol. 11 of *Lecture Notes in Computational Science and Engineering*, Springer Berlin Heidelberg, 197–208, doi: 10.1007/978-3-642-59721-3_14, 2000.

R. Olsen, Time-dependent boundary conditions for multiphase flow, Ph.D. thesis, Norwegian University of Science and Technology (NTNU), 2004.

M. Ainsworth, Dispersive and dissipative behaviour of high order discontinuous Galerkin finite element methods, J. Comput. Phys. 198 (1) (2004) 106–130, doi:10.1016/j.jcp.2004.01.004.

P. Lesaint, P. A. Raviart, On a Finite Element Method for Solving the Neutron Transport Equation, in: C. D. Boor (Ed.), Mathematical Aspects of Finite Elements in Partial Differential Equations, Academic Press, New York, 89–123, doi:10.1016/B978-0-12-208350-1.50008-X, 1974.

C. Omgba-Essama, Numerical Modelling of Transient Gas-Liquid Flows (Application to Stratified & Slug Flow Regimes), Ph.D. thesis, Cranfield University, 2004.